

Bayesian Inference of Frequency Specific Functional Connectivity in MEG Imaging Using a Spectral Graph Model

Huaqing Jin Farras Abdelnour Parul Verma
Benjamin S. Sipes Srikantan S. Nagarajan Ashish Raj †

Department of Radiology and Biomedical Imaging
University of California San Francisco, USA San Francisco, CA
† Correspondence to: ashish.raj@ucsf.edu

Abstract

Understanding the relationship between structural connectivity (SC) and functional connectivity (FC) of the human brain is an important goal of neuroscience. Highly detailed mathematical models of neural masses exist that can simulate the interactions between functional activity and structural wiring. These models are often complex and require intensive computation. Most importantly, they do not provide a direct or intuitive interpretation of this structure-function relationship. In this study we employ the emerging concepts of spectral graph theory to obtain this mapping in terms of graph harmonics, which are eigenvectors of the structural graph's Laplacian matrix. In order to imbue these harmonics with biophysical underpinnings, we leveraged recent advances in parsimonious spectral graph modeling (SGM) of brain activity. Here, we show that such a model can indeed be cast in terms of graph harmonics, and can provide closed-form prediction of FC in an arbitrary frequency band. The model requires only three global, spatially-invariant parameters, yet is capable of generating rich FC patterns in different frequency bands. Only a few harmonics are sufficient to reproduce realistic FC patterns.

We applied the method to predict FC obtained from pairwise magnitude coherence of source-reconstructed resting-state magnetoencephalography (MEG) recordings of 36 healthy subjects. To enable efficient model inference we adopted a deep neural network-based Bayesian procedure called simulation-based inference. Using this tool we were able to speedily infer not only the single most likely model parameters, but also their full posterior distributions. We also implemented several other benchmark methods relating SC to FC, including graph diffusion and coupled neural mass models. The present method was shown to give the best performance overall. Notably, we discovered that a single biophysical parameterization is capable of fitting FCs from all relevant frequency bands simultaneously, an aspect that not received adequate attention in prior computational studies.

Keywords: Bayesian; Connectomes; Functional connectivity; Magnetoencephalography; Spectral graph theory; Simulation-based inference

1 Introduction

A key goal in the neuroscience field is to understand the relationship between functional activity and the static anatomical structural wiring in the human brain [1, 2]. Many non-invasive neuroimaging techniques are used to measure functional activity, including functional magnetic resonance imaging (fMRI), electroencephalography (EEG), and magnetoencephalography (MEG) [3, 4]. The most common way in which this data are utilized is in the form of a functional connectivity (FC) matrix, which specifies the correlation between any two brain regions' measured activity time series [5, 6]. Although historically the field has focused on

8 fMRI-derived FC, it is now also possible to employ MEG time series to obtain FC; e.g. [7, 8] where the
9 authors find spatial agreement between FC measured using MEG and fMRI. Structural wiring is typically
10 obtained using diffusion tensor imaging (DTI) [9], followed by computational tractography to produce a
11 matrix of structural connectivity (SC) that gives the connection strength between all pairs of gray matter
12 regions [5, 10]. Hence a powerful way to understand the structure-function relationship in the brain is by
13 achieving a mapping between SC and FC.

14 Graph theory-based statistical relationships between SC and FC are well known phenomenologically
15 [11, 5, 12–20, 5, 21, 22, 6, 23–28]. Most such SC-FC studies pertain to fMRI, but increasingly are being
16 applied to M/EEG [29, 30]. It has recently emerged that *graph harmonics*, also known as *eigenvectors*,
17 *gradients* or *eigenmodes*, of the SC matrix, especially its Laplacian, are excellent graph features for mapping
18 this structure-function relationship. Indeed, the concept of graph harmonics, borrowing from the emerging
19 field of graph signal processing (GSP) [31–34], provide an elegant and concrete mathematical framework to
20 describe brain function and reflect distinct spatial patterns of functional signal [23, 35, 28]. It is of course not
21 necessary to employ *graph* harmonics; it has been shown that eigenmodes of signal propagation operators
22 in physical media (i.e. brain tissue), following its geometric boundaries, are also capable of producing
23 closed-form solutions and in reproducing FC [36]. The geometric eigenmode approach [37] is utilized for
24 both task-evoked and task-free fMRI data, suggesting that brain activity can be succinctly explained through
25 the brain’s geometry. However, it remains to be investigated whether this conclusion also applies to MEG
26 data. Despite these findings, graph theoretic methods may be preferable due to their simplicity and do not
27 require detailed knowledge of an individual brain’s geometric conformations.

28 The graph harmonics of SC and FC appear to be shared, and their eigenvalues reflect their graph frequency
29 [38, 39], and together they form a graph Fourier basis. Eigenvalues of FC are related by a function of SC
30 eigenvalues [40, 36, 41, 39, 42, 43], e.g. exponential [44] or power series [41, 40]. The explanatory power
31 of graph harmonics was further extended by Xie et al [27] who, by introducing conductance delays between
32 nodes, proposed a so-called "complex Laplacian" whose harmonics possessed rich spatial patterns that further
33 improved the structure-function correspondence. Remarkably, only a few SC graph harmonics are usually
34 sufficient to reproduce empirical fMRI-derived FC [35, 26, 45, 27]. Hence harmonics may be a natural
35 organizing principle for structure-function mapping, whereby low harmonics are thought to couple to global
36 or integrative functions, while high harmonics are uncoupled to function and subserve segregative functions
37 [46, 45]. The SC’s Laplacian harmonics may be thus thought of as the essential substrate on which functional
38 patterns of the brain are established [26, 35, 36, 45, 47, 27].

39 Unfortunately the explanatory power of graph harmonics is limited to a phenomenological level, since
40 they do not emerge from basic underlying biophysical processes, and are therefore unable to infer mechanistic
41 insights [48, 49]. Previously we and others showed that harmonics naturally arise from fMRI signal diffusion
42 or random walk through the SC graph [23, 42, 39], but passive diffusion is too simple to describe the rich and
43 oscillatory MEG signal. Historically, biophysical relevance necessitated detailed connectome-coupled neural
44 mass models (NMM) whose parameters reflect actual biophysical processes like excitatory and inhibitory
45 neuronal gains and capacitances, etc [50–60]. Such approaches involve massive time consuming non-linear
46 simulations. Thus the role of SC in these models is observed only indirectly, and does not allow a harmonic
47 decomposition of SC. Due to computational and interpretational challenges NMMs are not well suited to
48 reveal the key organizing role of graph harmonics in functional activity. Another conceptual limitation
49 is that the mapping between SC and FC is done separately for each frequency band of interest, whether
50 low-frequency *delta*, dominant *alpha* or high-frequency *beta*. Model parameters that best fit one band
51 typically do not fit another - this is problematic since the S-F coupling is a property of physical neural
52 systems and should not be frequency-band-dependent. While it is possible that the coupling may exhibit

53 an apparent frequency dependency, that dependency should come about from the model directly or from
54 modeling assumptions (e.g.frequency-dependent noise or coherence properties).

55 In this study we attempt to fill key conceptual and practical gaps in the field of brain graph harmonics and
56 their relationship to FC obtained from MEG recordings. We begin by establishing the relationship between
57 the eigenvalues of structural graph harmonics and those of FC. Then, we develop the theory necessary to
58 explain how graph harmonics emerge from basic biophysical processes on SC, leveraging recent advances in
59 modeling wideband MEG power spectra using the spectral graph model (SGM) [61, 9]. Note, although the
60 present harmonic model of FC retains the same biophysical principles as the SGM work, it is specifically
61 designed to predict narrow-band FC, not wideband power spectra. Despite the simplicity of the harmonic
62 decomposition, we show that indeed the proposed theory is imbued with all detailed biophysical processes
63 and parameters that have hitherto only been available via lengthy nonlinear NMM simulations. We show,
64 for the first time, that MEG FC from multiple frequency bands can be *simultaneously* decomposed into a
65 shared, parsimonious set (3-5) of low harmonics of SC. Remarkably, the proposed theory admits an analytical,
66 closed-form solution of MEG FC – a rare feature in comparison to extant NMMs which are only revealed via
67 large simulations. We then propose a speedy and flexible deep learning algorithm for inferring the biophysical
68 parameters that dictate the SC-FC relationship based on this harmonic decomposition. This tool allows us
69 to infer model parameters almost instantaneously for a given subject, after the network has been trained
70 on sufficient simulation-based training samples. Parameter inference has historically been an intractable
71 challenge in neural system modeling, and prior coupled NMMs require a combination of hand-tuning and
72 grid search [62, 63]. In contrast, we were not only able to obtain best-fit biophysical parameters very quickly
73 (within seconds) but also to give their full posterior distributions. The presented approach should also be
74 contrasted with another popular FC inference method called Dynamic causal modeling (DCM) [64, 65],
75 which seeks to estimate effective connectivity from functional activity, and does not employ an explicit
76 structure-function model as we do; see Discussion for further details.

77 We demonstrate this inference ability, critical for potential practical applications of model-based SC-FC
78 inference, on a study of 36 healthy individual subjects' MEG recordings. We achieved excellent predictive
79 power over *delta*, *theta*, *alpha*, and *beta* frequency bands, which favorably compared to several benchmark
80 methods, including prior graph harmonic mapping and SC-coupled NMM methods. Remarkably, we find
81 that a single biophysical parametrization is capable of simultaneously fitting FCs from all relevant frequency
82 bands. Thus our third key contribution is to show that the same underlying biophysical model and the same
83 graph harmonics can predict FC in all frequency regimes. By allowing for frequency dependency to emerge
84 from the underlying biophysics of neural activity, we resolve one of the key conceptual limitations of NMMs
85 – the biologically implausible inability of a single NMM model to fit to all FCs from all frequency bands
86 simultaneously.

87 This theoretical and experimental study attempts to combine both the elegance of graph harmonics and
88 the biophysical relevance of detailed NMMs. Thus the proposed method may be considered a "computational
89 microscope" into which high dimensional MEG data are funneled in to produce low-dimensional inferred
90 parameters that parsimoniously capture the SC-FC relationship. The latter may be further developed into
91 subject-specific biomarkers of mental or disease state. The demonstration that parsimonious, biophysical
92 harmonic-based SC-FC mapping can be achieved at near-instantaneous speed in individual subjects opens
93 new scientific and practical avenues for the emerging science of brain harmonics.

94 2 Theory and Model

95 Our goal of achieving a closed-form solution of functional connectivity (FC) and relating it to structural
96 connectivity necessitates a deterministic model of how neural activity, as measured by MEG recordings,
97 becomes established on the brain's structural connectome. For this purpose we leverage the spectral graph
98 model (SGM), first introduced in [61] and [9]. Our modeling effort begins from the SGM due to several
99 desirable properties. First, SGM is a linear biophysical model with a closed-form solution in the frequency
100 domain. Consequently, compared with non-linear neural mass models – where identifiability of model
101 parameter is not guaranteed [66, 49, 62], parameter inference with SGM is more tractable and faster. Prior
102 analyses [61, 9] show that SGM is able to recover the steady state wide-band frequency spectra as well as
103 the spatial patterns of the *alpha* frequency band obtained from MEG. Finally, SGM is highly parsimonious,
104 with only 7 global biophysically interpretable parameters while other biophysical models typically require
105 hundreds of spatially-varying parameters.

106 We begin this section by first describing the SGM in brief; the reader is referred to the original publications
107 for detailed derivations etc. It is emphasized that the prior SGM papers do not by themselves provide a recipe
108 or closed-form solution of FC, which is the focus of the current study and will be described in detail in the
109 subsequent section.

110 **Notation.** Scalar variables are denoted in normal font, while vectors and matrices are denoted in boldface.
111 Matrices are typically uppercase while vectors are typically lowercase. Matrix complex conjugate, transpose,
112 and Hermitian are denoted by $(\cdot)^*$, $(\cdot)^T$, and $(\cdot)^H$, respectively. The expectation is denoted by $\mathcal{E}(\cdot)$. Frequency
113 is denoted by angular frequency ω in radians per second and is related to frequency f in Hertz via $\omega = 2\pi f$.

114 2.1 Spectral graph modeling

115 Spectral graph model (SGM) is a hierarchical, linear, analytic model of brain oscillations, represented via
116 eigen-decomposition of the Laplacian of the structural connectivity matrix [61, 9]. In this sense it is an
117 exemplar of an emerging body of work on *harmonic models* of brain activity, whereby the latter is described
118 as a finite superposition of the brain network's harmonics or eigenvectors [23, 44, 35, 67, 68, 41, 40, 39].
119 In contrast to other harmonic-based models, the SGM provides an explicit wideband frequency response,
120 spanning low-frequency BOLD signal all the way to high-frequency MEG signal in the Gamma band [9]. A
121 typical SGM has two model layers, a mesoscopic layer for local neural circuits in the cortex and a macroscopic
122 layer for the whole brain, which accommodates the long-range fiber projections that connect individual
123 local circuits and neural populations. The model therefore explicitly lays out how the structural connectome
124 governs and mediates neural activity.

125 A salient feature of SGM is that it provides a closed-form solution of brain oscillations under the
126 frequency domain. Notably, the model can be fully characterized by only seven global parameters $\theta =$
127 $(\tau_e, \tau_i, g_{ei}, g_{ii}, \tau_g, v, \alpha)^T$. These include excitatory and inhibitory time constants τ_e, τ_i , and neural gains g_{ei}
128 and g_{ii} at the mesoscopic level; and long-range excitatory time constant τ_g , speed v , coupling constant α
129 at the macroscopic level. We define the complex Laplacian matrix $\mathcal{L}(\omega; \alpha, v) = \mathbf{I} - \alpha \mathbf{C}^*(\omega; v)$ where the
130 elements of \mathbf{C}^* are $c_{ij}^*(\omega; v) = c_{ij} \exp(-j\omega\tau_{ij}^v)$, $i, j = 1 \dots N$, where c_{ij} is the structural connectivity
131 between regions i and j and τ_{ij}^v corresponds to the delay due to a finite speed v , which is calculated for every
132 region as the distance between regions divided by the speed v . As derived in [61, 9], the frequency domain
133 solution of the macroscopic signals is given in closed form as

$$\mathbf{X}(\omega) = \left(j\omega \mathbf{I} + \frac{1}{\tau_g} F_g(\omega) \mathcal{L}(\omega) \right)^{-1} H_{\text{local}}(\omega) \mathbf{P}(\omega), \quad (1)$$

where $F_g(\omega)$ is the Fourier transform of a Gamma-shaped neural response function $f_g(t; \tau_g)$ that seeks to model the macroscopic transfer function of excitatory projection neurons, with characteristic time constant τ_g . The function $H_{\text{local}}(\omega; \tau_e, \tau_i, g_{ei}, g_{ii})$ represents the transfer function capturing the overall activity of populations of excitatory and inhibitory neurons at the local or mesoscopic level. SGM allows for fitting local transfer function to each region; however, it was previously shown that this is not necessary and that a spatially-invariant set of mesoscopic parameters is sufficient to recapitulate empirical MEG power spectra [61]. The entire model is driven by external or region-specific process $\mathbf{p}(t)$, whose Fourier transform is denoted $\mathbf{P}(\omega)$ above.

Factoring $\mathcal{L}(\omega)$ into its eigen components $\mathcal{L}(\omega) = \mathbf{U}(\omega) \boldsymbol{\Lambda}(\omega) \mathbf{U}^H(\omega) = \sum_{k=1}^N \lambda_k(\omega) \mathbf{u}_k(\omega) \mathbf{u}_k^H(\omega)$, we can write equation (1) as an expansion on the harmonics of \mathcal{L} :

$$\mathbf{X}(\omega) = \sum_{k=1}^N \frac{\mathbf{u}_k(\omega) \mathbf{u}_k^H(\omega)}{j\omega + \tau_g^{-1} \lambda_k(\omega) F_g(\omega)} H_{\text{local}}(\omega) \mathbf{P}(\omega). \quad (2)$$

For reference, a detailed derivation is given in the accompanying Supplementary Information section.

2.2 Deriving a closed-form expression for cross-spectral density of SGM

Prior use of SGM has focused on obtaining the neural signal equation in the frequency domain and determining its power spectrum. Here we propose to explicitly derive the *structure-function relationship*, i.e. the 2nd order statistics of the signal \mathbf{X} in terms of the eigendecomposition of the structural Laplacian \mathcal{L} . There are several equivalent ways to achieve this; here we use the most intuitive approach, starting with a definition of the cross-spectral density (CSD) as the expectation $\mathcal{E}(\mathbf{X}(\omega) \mathbf{X}^H(\omega))$. Let us rewrite equation (2) more succinctly as $\mathbf{X}(\omega) = \mathbf{U}(\omega) \boldsymbol{\Gamma}(\omega) \mathbf{U}^H(\omega) H_{\text{local}}(\omega) \mathbf{P}(\omega)$, where the diagonal matrix $\boldsymbol{\Gamma}(\omega)$ has as its k -th diagonal entry $\gamma_k(\omega) = \frac{1}{j\omega + \tau_g^{-1} \lambda_k(\omega) F_g(\omega)}$. Note that the model is dependent on a given instantiation of the model parameters $\boldsymbol{\theta}$; for convenience, this dependence is not shown above but is always to be assumed implicitly. Using this shorthand we expand the CSD of $\mathbf{X}(\omega)$ as:

$$\mathcal{E}(\mathbf{X}(\omega) \mathbf{X}^H(\omega)) = |H_{\text{local}}(\omega)|^2 \mathbf{U}(\omega) \boldsymbol{\Gamma}(\omega) \mathbf{U}^H(\omega) \mathcal{E}(\mathbf{P}(\omega) \mathbf{P}^H(\omega)) \mathbf{U}(\omega) \boldsymbol{\Gamma}^H(\omega) \mathbf{U}^H(\omega)$$

Now, we introduce the key assumption that *the driving input signal is uncorrelated across regions and across time*. This is plausible because we are interested in achieving the resting-state stationary description of FC, where no external stimulation is provided to the brain. In this scenario, the driving signal is internal to the brain, and while those internal processes may have spatial heterogeneity at specific instances, over time those reflect simply as spatially and temporally uncorrelated noise processes. With this assumption or approximation we have $\mathcal{E}(\mathbf{P}(\omega) \mathbf{P}^H(\omega)) = \sigma^2 \mathbf{I}$ for an i.i.d. noise process with variance σ^2 . Since the harmonics or eigenvectors are orthonormal, we have $\mathbf{U}^H(\omega) \mathbf{U}(\omega) = \mathbf{I}$, and the right hand side of the above equation greatly simplifies to $\sigma^2 |H_{\text{local}}(\omega)|^2 \mathbf{U}(\omega) |\boldsymbol{\Gamma}(\omega)|^2 \mathbf{U}^H(\omega)$.

Additionally, the estimated FC is subsequently normalized via its diagonal terms, which eliminates the variance σ^2 and local frequency response function $H_{\text{local}}(\omega)$, which no longer need to be inferred.

165 Thus, finally, we have a closed-form solution of the CSD $\widehat{\mathbf{F}}(\omega)$ at any frequency, as a superposition over
 166 graph harmonics:

$$\widehat{\mathbf{F}}(\omega, \boldsymbol{\theta}_{reduced}) = \sum_{k=1}^N \frac{\mathbf{u}_k(\omega) \mathbf{u}_k^H(\omega)}{|j\omega + \tau_g^{-1} \lambda_k(\omega) F_g(\omega)|^2} \quad (3)$$

167 Note, the theoretical FC is now dependent on a reduced set of model parameters, since due to the
 168 elimination of $H_{local}(\omega)$ term, the estimated FC from SGM only depends on the 3-parameter reduced vector
 169 $\boldsymbol{\theta}_{reduced} = (\tau_g, v, \alpha)$.

170 Thus, the theoretical FC of the SGM is given by a superposition of graph Laplacian eigenmodes
 171 or harmonics $\mathbf{u}_k(\omega)$, each of which manifests a frequency response $\gamma_k(\omega)$ dependent on the eigenvalue
 172 $\lambda_k(\omega)$. The eigenvectors of the predicted FC are identical to those of the structural Laplacian. In this
 173 manner we have reduced the full cross-spectral density of brain activity to modeling just the diagonal
 174 eigenvalues of the structural connectome; all region-pair coherences are thus expected to be captured entirely
 175 by the eigenvectors $\mathbf{U}(\omega)$. This description is entirely consistent with prior studies using graph harmonics
 176 [23, 44, 35, 67, 68, 41, 40, 39], but in contrast to those studies, here we provide for the first time a fully
 177 frequency-resolved description of FC, at arbitrary frequency. Remarkably, this description is direct, and does
 178 not require either simulations in time, or indirect calculation of FC via the narrow-band Hilbert envelope
 179 [56, 68].

180 3 Methods

181 3.1 Dataset

182 In this work we analyse magnetoencephalography (MEG) data. The dataset is based on preprocessed and
 183 publicly available dataset for the SGM work [69], and is identical to the one used for the modified SGM
 184 [9]. The MEG datasets and the corresponding SC and distance matrices were all processed at the regional
 185 level under the Desikan–Killiany atlas parcellation with 68 cortical regions [70]. For this dataset, MEG,
 186 anatomical MRI, and diffusion MRI were collected for 36 healthy adult subjects (23 males, 13 females; 26
 187 left-handed, 10 right-handed; mean age 21.75 years, with age range 7 – 51 years). Data collection procedure
 188 has been described previously [61]. All study procedures were approved by the institutional review board at
 189 the University of California at San Francisco and were in accordance with the ethics standards of the Helsinki
 190 Declaration of 1975 as revised in 2008. MEG recordings were collected for 5 minutes while the subjects
 191 were resting and had eyes closed. Out of the 5 minute recording, a 1 minute snippet was chosen which was
 192 deemed most noise free. MRI followed by tractography was used to generate the connectivity and distance
 193 matrices. The entry in the distance matrix is the fiber length distance, which is defined as the average number
 194 of voxels spanned across all streamlines between those regions. The publicly available dataset consisted of
 195 processed connectivity and distance matrices for every subject.

196 For details on the data processing, refer to Section S.1 of the supplementary materials as well as the
 197 previous literature [61, 9, 71].

198 3.2 Constructing functional connectivity (FC) in discrete frequency bands

199 This study requires the fitting of a FC matrix derived from the theoretical cross-spectral density (Eq 3) to
 200 empirical MEG-derived FC, specifically its inter-regional coherence. We therefore evaluated FC at four

201 commonly studied MEG frequency bands *delta* (2 – 3.5 Hz), *theta* (4 – 7 Hz), *alpha* (8 – 13 Hz) and *beta*
 202 (13 – 20 Hz).

203 Since the SGM was tailored to frequencies up to ≈ 25 Hz, we only investigate the results on the lower part
 204 of the *beta* band (i.e., 13 – 20 Hz). The SGM model is designed for frequencies up to around 25 Hz because
 205 our SGM model can accurately reconstruct the PSD below 25 Hz, i.e. the *beta* band. Higher frequencies,
 206 in the *gamma* band, arise mainly from local neural populations that do not appear to be modulated by the
 207 structural connectivity, hence a conenctome-based model like SGM would not be expected to fit spectra in
 208 this regime, as noted in prior reports [61, 9, 71].

209 In order to convert the theoretical CSD to band-specific FC, we first summed the CSD across all
 210 frequencies within a given band, then normalized its rows and columns by the diagonal. E.g. for the
 211 *alpha*-band we define

$$\hat{\mathbf{F}}_{\text{alpha}}(\boldsymbol{\theta}_{\text{reduced}}) = \Delta^{-1/2} \int_{\omega \in \Omega_{\text{alpha}}} \hat{\mathbf{F}}(\omega, \boldsymbol{\theta}_{\text{reduced}}) d\omega \quad \Delta^{-1/2}. \quad (4)$$

212 where Δ contains the diagonal entries of the band-sum $\int \hat{\mathbf{F}}(\omega) d\omega$ and Ω_{alpha} contains the range of
 213 frequencies within the *alpha* band. Analogously, we define $\hat{\mathbf{F}}_{\text{delta}}$, $\hat{\mathbf{F}}_{\text{theta}}$ and $\hat{\mathbf{F}}_{\text{beta}}$; generically, we will
 214 refer to a given band's FC as $\hat{\mathbf{F}}_{\text{band}}$.

215 Empirical FC matrices using MEG data were constructed analogously to the theoretical ones, using
 216 coherence-based analysis implemented in the MNE-Connectivity 0.4.0 Python toolbox [72]. Denoting
 217 the Fourier transform of two time series for i^{th} and j^{th} ROIs as $Y_i(\omega)$ and $Y_j(\omega)$, the i, j -th entry of coherence-
 218 based FC for a given frequency band, say *alpha*, is given by

$$[\mathbf{F}_{\text{alpha}}]_{i,j} = \frac{\left| \int_{\omega \in \Omega_{\text{alpha}}} Y_i^*(\omega) Y_j(\omega) d\omega \right|}{\left| \int_{\omega \in \Omega_{\text{alpha}}} Y_i(\omega) d\omega \right| \left| \int_{\omega \in \Omega_{\text{alpha}}} Y_j(\omega) d\omega \right|} \quad (5)$$

219 It may be verified that both the theoretical and empirical FCs are analogous to coherence, and normalized
 220 in the same manner. In this work, we set the diagonal elements of both theoretical and empirical FC to
 221 zero following the convention. Our implementation replaces the integration above by summation over ten
 222 equally-spaced frequency points per band. We used the `spectral_connectivity_epochs` function
 223 from the MNE-Connectivity Python package [73], set to 100 epochs, to obtain the FCs from the MEG
 224 recordings for each frequency band. Specifically, this function firstly filters the MEG time series into the
 225 desired frequency band, then computes the coherence matrix for each epoch, and finally averages the matrices
 226 across epochs to obtain the FC matrix. Epochs are equal-duration time segments of the EEG/MEG signal
 227 during each of which the signal may be considered relatively stationary [73]. Thus, the use of a single
 228 epoch reflects that the FC networks were obtained from the entire temporal signal, while > 1 epochs involve
 229 segmenting the time series and combining each segment's FC together in a principled manner. The mode
 230 was set to `multitaper`, an option that has favorable time-frequency product and a more optimal trade-off
 231 between bias and variance of spectral estimates. No frequency windowing was applied (`mt_windowing`).

232 3.3 Simulation-based inference for FC

233 Despite the parsimony and explicit solution of the SGM, its inference from empirical FC is quite challenging
 234 using sampling or gradient descent methods. Simulation-based inference (SBI) [74] is a recent advanced
 235 neural network-based tool that makes Bayesian inference possible for models with complex and stochastic

236 simulators. This technique is especially attractive in situations where the likelihood function is intractable or
 237 difficult to compute, where other methods based on explicit formulation of the likelihood function become
 238 challenging. It shows some success in identifying mechanistic models of neural dynamics [75] and especially
 239 presents promising results for predicting power spectral density with SGM model for MEG data [71].

240 Here we adapt and apply the SBI tool to fit the SGM model to empirical FC from selected frequency bands
 241 of MEG recordings (referred to as SGM-SBI). SBI requires the forward computation of a large number of
 242 simulations, in order to assemble a set of paired samples for training. Therefore we first compute, for any pa-
 243 rameter choice $\theta_{reduced}$ drawn from a suitably defined prior distribution, the pair $(\theta_{reduced}, \hat{\mathbf{F}}_{band}(\theta_{reduced}))$
 244 for each frequency band $band \in \{delta, theta, alpha, beta\}$, using the SGM equations (3) and (4). Subse-
 245 quently, noise from a standard Gaussian distribution is added to each entry of the computed mean FC matrix
 246 to account for the inherent noise in the empirical FC [71].

247 *Parameter transformation.* Any biophysical model with physically-realisable parameters typically admits
 248 well-defined parameter ranges beyond which the parameters and the overall model becomes implausible. The
 249 SGM too is a biophysical model whose parameters have well-defined biological meaning, and whose ranges
 250 can be specified *a priori* - see Table 1. These ranges are taken from previous SGM works [9, 61, 71]. The
 251 bounded parameter constraints cause difficulties for posterior sampling with SBI [76], we re-parameterize
 252 SGM parameters to ease the posterior sampling. Specifically, SGM parameters are transformed with a
 253 standard logit function $s = \mathcal{H}(\theta_{reduced})$ so that the original lower and upper bounds map to $-\infty$ and $+\infty$,
 254 respectively [71].

255 *Prior specification.* To obtain the satisfactory inference performance with SBI, a large training sample
 256 size is typically required. To ease the computational burden, we construct informative priors derived from
 257 the dual annealing fitting results to improve the quality of the simulated samples in the current study. With
 258 better quality samples, the simulated sample size can be significantly reduced and the neural network can
 259 learn the posterior distribution more effectively. To be specific, we firstly fit the theoretical and empirical FCs
 260 with the dual annealing algorithm with 200 iterations yielding the rough point estimate of SGM parameters,
 261 \hat{s}_{ANN} . We adopt a Gaussian prior $\pi(s) \sim N(\hat{s}_{ANN}, \mathbf{I})$ for the transformed parameters, where \mathbf{I} represents
 262 the identity matrix.

263 *Training procedure.* We adopt a 3-round training process. Initially, 1000 pairs of $(s, \hat{\mathbf{F}}_{band}(\mathcal{H}^{-1}(s)))$ are
 264 generated using SGM and prior $\pi(s)$. These pairs are then used to train a neural network, parametrized by
 265 Φ , whose task it is to approximate the true posterior of s via a neural spline flow q_Φ [77]. Neural network
 266 architecture including 50 hidden features use the 2-block residual net for context embedding, which is the
 267 default setting in the `sbi` package [74]. All other hyperparameters also adopt the default settings. We feed
 268 the empirical FC \mathbf{F}_{band} to q_Φ , yielding the posterior distribution $q_\Phi(s|\mathbf{F}_{band})$ with estimated parameter $\hat{\Phi}$
 269 for the first round. In the subsequent training round, we update parameters Φ in a similar manner. The only
 270 variation is that we use the previous round's posterior distribution as the current round's prior distribution
 271 for generating simulation pairs. After 3-round training, the final estimation of the posterior $q_\Phi(s|\mathbf{F}_{band})$ is
 272 obtained. The target posterior distribution of $\theta_{reduced}$ is $q_{\hat{\Phi}} \times |\det(\mathbf{J})|$ where \mathbf{J} is the Jacobian matrix of
 273 the transformation function \mathcal{H} [78]. The process of obtaining the posterior distribution of s is delineated in
 274 Algorithm 1. A more comprehensive illustration of the combination of SBI with SGM can be found in [71].

275 We also consider training jointly with all four bands, where the corresponding FCs are simply stacked into
 276 a larger matrix $\mathbf{F}_{shared} = (\mathbf{F}_{delta}^T \mathbf{F}_{theta}^T \mathbf{F}_{alpha}^T \mathbf{F}_{beta}^T)^T$, and analogously we define the larger theoretical
 277 FC matrix $\hat{\mathbf{F}}_{shared}(\theta_{reduced})$. Then the above algorithm is applied to these larger "all-bands" FCs, following
 278 which we infer the posterior of a single set of parameters θ_{shared} that can simultaneously fit to all bands
 279 (referred to as SGM-SBI-shared).

Algorithm 1 Posterior estimation from FC with SBI

Require: An initial multivariate Gaussian prior $\pi(\mathbf{s}) \sim \mathcal{N}(\hat{\mathbf{s}}_{\text{ANN}}, \mathbf{I})$, a specific frequency band $band \in \{\text{delta, theta, alpha, beta}\}$, SGM model $\widehat{\mathbf{F}}_{band}(\mathcal{H}^{-1}(\mathbf{s}))$, an observation \mathbf{F}_{band} , the number of samples per round $M = 1000$.

for $r = 1, 2, 3$ **do**

- for** $m = 1, \dots, M$ **do**
- Sample $\mathbf{s}_m \sim \pi(\mathbf{s})$
- Compute SGM forward model $\widehat{\mathbf{F}}_{band}^{(m)}(\mathcal{H}^{-1}(\mathbf{s}_m))$
- end for**
- $\widehat{\Phi} \leftarrow \underset{\Phi}{\text{argmin}} - \frac{1}{M} \sum_{m=1}^M \log \left\{ q_{\Phi}(\mathbf{s}_m | \widehat{\mathbf{F}}_{band}^{(m)}) \right\}$
- $\pi(\mathbf{s}) \leftarrow q_{\widehat{\Phi}}(\mathbf{s} | \mathbf{F}_{band})$
- end for**
- return** $q_{\widehat{\Phi}}(\mathbf{s} | \mathbf{F}_{band})$ as the estimate of the posterior distribution of \mathbf{s} . The posterior distribution of θ_{reduced} is $q_{\widehat{\Phi}} \times |\det(\mathbf{J})|$, where \mathbf{J} is the Jacobian matrix of the transformation \mathcal{H} .

Table 1: Global SGM parameters and bounds for parameter estimation for SBI-SGM

Name	Symbol	Lower/upper bound
Graph time constant	τ_g	[0.005 s, 0.03 s]
Transmission speed	v	[5.0 m/s, 20.0 m/s]
Long-range connectivity coupling constant	α	[0.1, 1]

280 **3.4 Metrics of performance**

281 To better evaluate the performance of our SGM-SBI pipeline in FC, we introduce three main metrics to assess
282 the similarity between estimated and empirical FCs, including the Pearson’s correlation, Lin’s correlation [79]
283 and mean square error (MSE). Lin’s correlation (or concordance correlation coefficient) is a reproducibility
284 index which has been used in the neuroimaging area [80] for a long time. While Pearson’s correlation
285 only cares about the dependence between two variables, it further considers the deviation of the means and
286 variances of the two variables. Thus, it can be regarded as a stricter version of Pearson’s correlation. The
287 value of Lin’s correlation is within $[-1, 1]$ where a larger value indicates higher consistency.

288 While the interpretation of the values of Pearson’s correlation is straightforward, the values of Lin’s
289 correlation and MSE lack intuitive understanding. Therefore, instead of the raw Lin’s correlation and MSE,
290 we report the corresponding standardized versions. To be specific, we randomly shuffle the empirical FC for
291 1000 times and calculate the metrics between the shuffled versions and original one. Lin’s correlation and
292 MSE are then standardized using the mean and variance derived from the shuffled metrics.

293 **3.5 Comparison with benchmark methods**

294 In order to compare the present SGM-SBI method for mapping FC from SC, we implemented several current
295 and relevant benchmark methods. All benchmarks, described below, were applied to the same datasets as the

296 proposed method, and were evaluated using the same performance metrics. The benchmark methods were:

- 297 1. *Direct mapping.* We used the subject's SC itself as a direct prediction of their FC, measuring its
298 performance using measures of correlation, Lin concordance and MSE applied element-wise between
299 the two matrices SC and FC.
- 300 2. *Eigen-mapping.* Recent work [23, 44] shows that FC is predictable from the eigendecomposition of
301 SC via a simple graph diffusion model. In the harmonics space this amounts to a simple relationship
302 between the eigenvalues of FC and SC Laplacian, e.g. the exponential decay function. Hence we
303 employed the two-parameter exponential relationship suggested by[44] i.e.,

$$\lambda_{\text{eig}} = \exp(-\lambda_{\text{sc}} * p_1) + p_2,$$

304 where (p_1, p_2) are the parameters that need fitting and λ_{eig} and λ_{sc} are the eigenvalues of estimated FC
305 from the eigen-mapping and SC, respectively.

- 306 3. *Coupled NMM.* We adopt the Wilson-Cowan (WC) model [81] as our NMM. To model the coupling
307 between difference brain regions, the WC model includes the input from other ROIs during its evolution.
308 Specifically, denoting $E(i, t)$ and $I(i, t)$ as the number of excitatory and inhibitory cells firing at ROI i
309 and time t , the model is

$$\begin{aligned} \tau_e \frac{E(i, t)}{dt} &= -E(i, t) + \{1 - E(i, t)\} S_e \{c_{ee}E(i, t) - c_{ie}I(i, t) + O(i, t) + P(i, t)\} + \epsilon_e(i), \\ \tau_i \frac{I(i, t)}{dt} &= -I(i, t) + \{1 - I(i, t)\} S_i \{c_{ei}E(i, t) - c_{ii}I(i, t) + Q(i, t)\} + \epsilon_i(i), \end{aligned}$$

310 where $O(i, t)$ is the input from other ROIs, τ_e and τ_i are the time constants, S_e and S_i are functions
311 of sigmoid form, $(c_{ee}, c_{ie}, c_{ei}, c_{ii})$ are local coupling parameters, $P(i, t)$ and $Q(i, t)$ are the external
312 input to the excitatory/inhibitory populations, $\epsilon_e(i)$ and $\epsilon_i(i)$ are the noise. We implement the NMM
313 with `neurolib` package in python [82]. NMM is fitted with the evolutionary algorithm over 4
314 parameters, global coupling strength, the baseline external input parameters (used to generate $P(i, t)$
315 and $Q(i, t)$) and the global noise intensity. The simulation duration is set to 61,000 ms. For more
316 detailed information on the implementation of the WC model, please refer to (Cakan et al., 2021)[82].

317 It is worth noting that the numbers of parameters in SGM-SBI, NMM and eigen-mapping method are
318 3, 4 and 2 respectively, which are overall comparable. All benchmark methods above were fitted to and
319 evaluated with Lin's correlation loss. For the fitting process, we convert the FC matrix into a vector and apply
320 the minmax operator on this vector for both SBI-SGM and NMM. However, in the case of the eigen-mapping
321 method, we refrain from using the minmax operator as it prevents convergence. All performance metrics are
322 computed with the vectorized FC following minmax operator. For all the methods, the SCs are pre-processed
323 in identical ways, including removing the extreme connections via capping large values and adding minor
324 values to enhance the connection between the corresponding regions between left and right hemispheres.
325 These pre-processing steps are consistent with the previous work [9, 61] and are robust to different datasets
326 and choice of atlas.

327 4 Results

328 4.1 SGM model produces rich FC patterns depending on parameters and frequency bands

329 We first need to establish that the proposed SGM model is capable of producing a rich diversity of FCs that
330 can change depending on frequency band and model parameters. We varied a single SGM parameter, in turn,

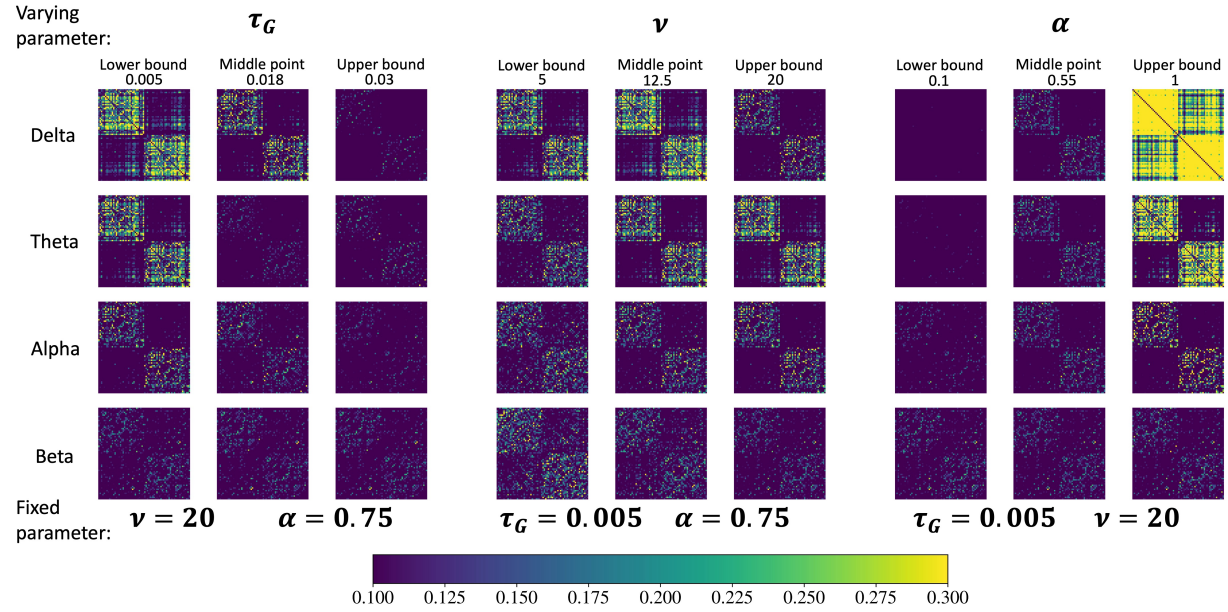


Figure 1: The SGM-modelled FCs in *delta*, *theta*, *alpha* and *beta* bands when varying τ_G (left), ν (middle) and α (right) and fixing the other two parameters, separately. Note that each column of FCs shares the same SGM parameters. The fixed parameters are set to the fitted value from SGM-SBI-shared, while the varying parameters fluctuate within the range specified in Table 1. The values of three parameters are shown in the figure.

331 in the range given in Table 1 while fixing the other two at the optimal values fitted on empirical data. The
332 predicted FCs are shown in Figure 1. All three SGM parameters influence the resulting FCs. However, their
333 effects can vary significantly across different frequency bands. In *delta* and *theta* bands, each parameter
334 noticeably affects overall connectivity strength as well as inter- and intra-hemispheric connectivity. Model
335 FCs generally exhibit denser and stronger connections within hemisphere and weaker connections between
336 hemispheres. In *alpha* band, τ_G and α exert substantial influence within each hemisphere, while speed v
337 predominantly affects inter-hemispheric connectivity. In *beta* band, τ_G and α show minor effect on the FCs
338 while increasing v reduces overall connectivity. Overall, the highest predicted FC is seen in lower frequencies,
339 while *beta* band gives the lowest FC. Most importantly, *the same model, with fixed parameters, is capable*
340 *of producing diverse FC patterns in different frequency bands*. The requirement that the same biophysical
341 process be capable of producing frequency-specific FC, was one of the key motivations of this study.

342 **4.2 SC Harmonics encompass spatial gradients of MEG FC**

343 Since the proposed SGM model is fundamentally based on the utility of SC harmonics to capture functional
344 activity patterns, we first show in Figure 2A the real components of the first 3 harmonics \mathbf{u}_1 to \mathbf{u}_3 on the
345 brain surface. These harmonics, averaged across 36 subjects, are normalized within a range of $[-1, 1]$. The
346 first harmonic represents a global spatial pattern, previously suggested to represent the global signal in fMRI
347 [44]. The second harmonic manifests a strong left-right spatial gradient and appears to capture the prominent
348 interhemispheric functional connectivity structure. It also has a prominent internal structure with high levels
349 in temporal and orbitofrontal areas lower levels in medial and motor areas. Given that the brain plots exhibit
350 similarity across various frequency bands, we have chosen to present plots from only one band. The third
351 harmonic is laterally symmetric and captures a strong anterior-posterior gradient such that visual areas are at
352 one pole and dorsolateral and orbitofrontal areas at the opposite pole. This finding is consistent with previous
353 studies [27, 35].

354 **4.3 Top few SC harmonics capture most of the energy of MEG FC**

355 We evaluated the projections of the MEG-derived FC matrix \mathbf{F}_{band} on the complex Laplacian harmonics \mathbf{U} ,
356 i.e. $\text{diag}(\mathbf{U}^H \mathbf{F}_{band} \mathbf{U})$. The moduli of diagonal elements of this matrix contain the amount of MEG FC that
357 is captured within each harmonic. Let us refer to this quantity as a harmonic's "participation energy". The
358 relationship between the SC harmonics' participation energy in MEG FC and the moduli of their associated
359 eigenvalues are shown in Figure 2B, separately for each frequency band *delta*, *theta*, *alpha* and *beta*.
360 Each curve corresponds to a single subject. In producing these plots, the Laplacian matrix was evaluated
361 at each band's mean frequency, e.g. frequencies [2.75, 5.5, 10.0, 16.5] Hz. Across all bands, the MEG FC
362 appears to be well captured by only the first few harmonics, roughly \mathbf{u}_1 to \mathbf{u}_3 . It is closely related to the
363 observation in [83], where the authors showed that low order brain surface eigenmodes carry most of the
364 energy. Interestingly, the eigenvalue relationship appears to follow roughly the exponential decay function
365 proposed by our group on fMRI data based on graph diffusion arguments [23]. This exponential relationship is
366 well established now for fMRI FC but has not previously been demonstrated for MEG data. Nonetheless, there
367 are many deviations from a strict exponential curve, especially in the 2nd and 3rd harmonics' participation
368 energy.

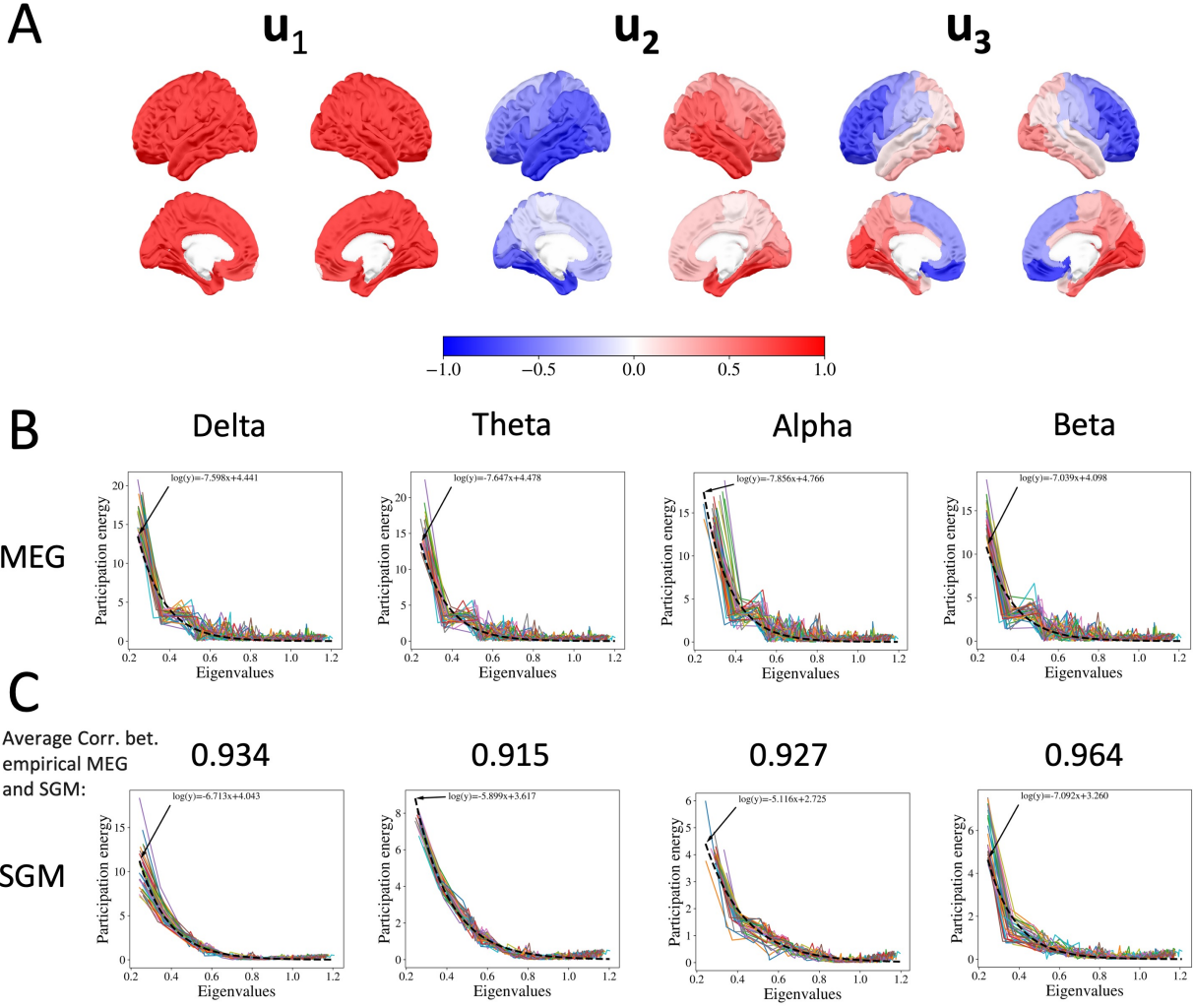


Figure 2: **A:** The real part of first three complex Laplacian eigenvectors at the *alpha* band averaged on 36 subjects plotted on the brain. **B:** The participation energy of empirical FCs after projecting them on the complex Laplacian eigenvectors versus the moduli of Laplacian eigenvalues from *delta*, *theta*, *alpha* and *beta* bands. The black dashed lines represent the exponential decay function fitted to the participation energy of empirical FCs. **C:** The participation energy of SGM-estimated FCs after projecting them on the complex Laplacian eigenvectors versus the moduli of Laplacian eigenvalues from *delta*, *theta*, *alpha* and *beta* bands (same order as panel B). The black dashed lines represent the exponential decay function fitted to the participation energy of empirical FCs. The number above each plot is the average Pearson's correlation between participation energies from MEG and SGM across 36 subjects. Since SGM is capable of giving wideband spectra, each harmonic can have a different participation energy at different frequencies. Hence we show each frequency band's participation energy in separate plots. The participation energy is defined as the moduli of diagonal elements of the projections of the FCs on the complex Laplacian harmonics, i.e., $\text{diag}(\mathbf{U}^H \mathbf{F} \mathbf{U})$. Each curve represents a single subject. The empirical and theoretical participation energy curves show striking similarities with exceptionally high Pearson's correlations (above 0.9 for all four bands).

369 **4.4 SGM model recapitulates the eigenvalue relationship between SC and MEG FC**

370 Next we assessed whether the theoretical SGM model manifests a similar harmonic decomposition. To
371 do this we obtained the participation energies of all harmonics for the model-predicted FC $\hat{\mathbf{F}}_{band}$ given
372 by: $\text{diag}(\mathbf{U}^H \hat{\mathbf{F}}_{band} \mathbf{U})$. We chose the mean posterior SGM parameters from the band-specific SGM-SBI
373 to produce the predicted FC in each band; detailed results of model fitting are contained in later sections.
374 The resulting plots across all bands is in Figure 2C where the Pearson's correlation between participation
375 energies from MEG and SGM is shown above each plot. The empirical and theoretical participation energy
376 curves show striking similarities with exceptionally high Pearson's correlations (above 0.9 for all four bands),
377 and a very similar relationship to harmonic eigenvalues, with a roughly exponential function with some
378 deviations. Across all four bands, it is evident that the participation energy curves obtained from SGM-SBI
379 model-predicted FC closely approximate those derived from empirical FCs - a clear validation of the graph
380 harmonic model's ability to accurately approximate empirical FCs. Interestingly, the model FC's participation
381 energy curve suggests that it requires a few more harmonics, up to 4 or 5, to capture overall FC energy.
382 Nonetheless, a small fraction of harmonics are sufficient to capture most of the participation energy of
383 model-predicted FC. Both empirical and model FC appear to be dominated by the first 3 graph harmonics. It
384 is remarkable that a combination of these 3 canonical structural harmonics are capable of capturing most of
385 the participation energy of both empirical MEG and model-predicted FC.

386 **4.5 Empirical and fitted model's FC matrices**

387 The mean FC matrices across all subjects, obtained via MNE-Connectivity toolbox from MEG time
388 series using the absolute coherence method (see subsection 3.2) for all four bands, are illustrated in Figure 3
389 (middle column) as matrix heatmaps. Each matrix has rows and columns corresponding to brain regions, and
390 elements of the matrix represent the functional connectivity between the two corresponding regions. Empirical
391 FC in all bands appear largely consistent, each displaying strong intra-hemispheric but commensurately
392 weaker inter-hemispheric coherence. There is evidence of modular structure within each hemisphere as well.
393 Note that the diagonal was removed for visualization, since self-connectivity is trivially and always equal to 1
394 in FC by definition. The frequency bands are defined as: *delta*, [2, 3.5] Hz, *theta*, [4, 7] Hz, *alpha*, [8, 12]
395 Hz, and *beta*, [13, 20] Hz.

396 For each band and each subject, we fitted the theoretical SGM model to the empirical one to obtain
397 the optimal band-specific SGM parameters $\{\tau_g, v, \alpha\}$. These parameters were then used to calculate the
398 estimated FCs via Eq 3. The left column shows the mean estimated FC obtained from all subjects. Similar to
399 the empirical FCs results, the estimated FCs with band-specific parameters exhibit a consistent pattern across
400 different bands, i.e., higher connectivity within hemispheres and lower connectivity between hemispheres.
401 However, when compared to empirical FCs, the estimated FCs have stronger connectivity within hemispheres
402 while weaker connectivity between hemispheres. Moreover, as the frequency of the band increases, there is a
403 significant decrease in the overall density of the estimated FC. This could be partially attributed to the SGM's
404 design, wherein no attempt was made to capture higher frequencies in the high *beta* and *gamma* bands,
405 which are thought to arise from local oscillatory processes that are not directly modulated by the whole brain
406 connectome [61, 9, 71].

407 We also explored a variant of SGM-SBI, where we fitted the theoretical FCs from all 4 bands with a single
408 set of band-shared SGM parameters for each subject. The resulting FCs, referred to as SGM-SBI-shared,
409 are depicted in the rightmost column. The estimated FCs from band-shared parameters closely resemble
410 those from band-specific ones across all four bands. This implies that a single set of SGM parameters can
411 successfully duplicate the MEG FCs across all four frequency bands, suggesting, uniquely in the literature on

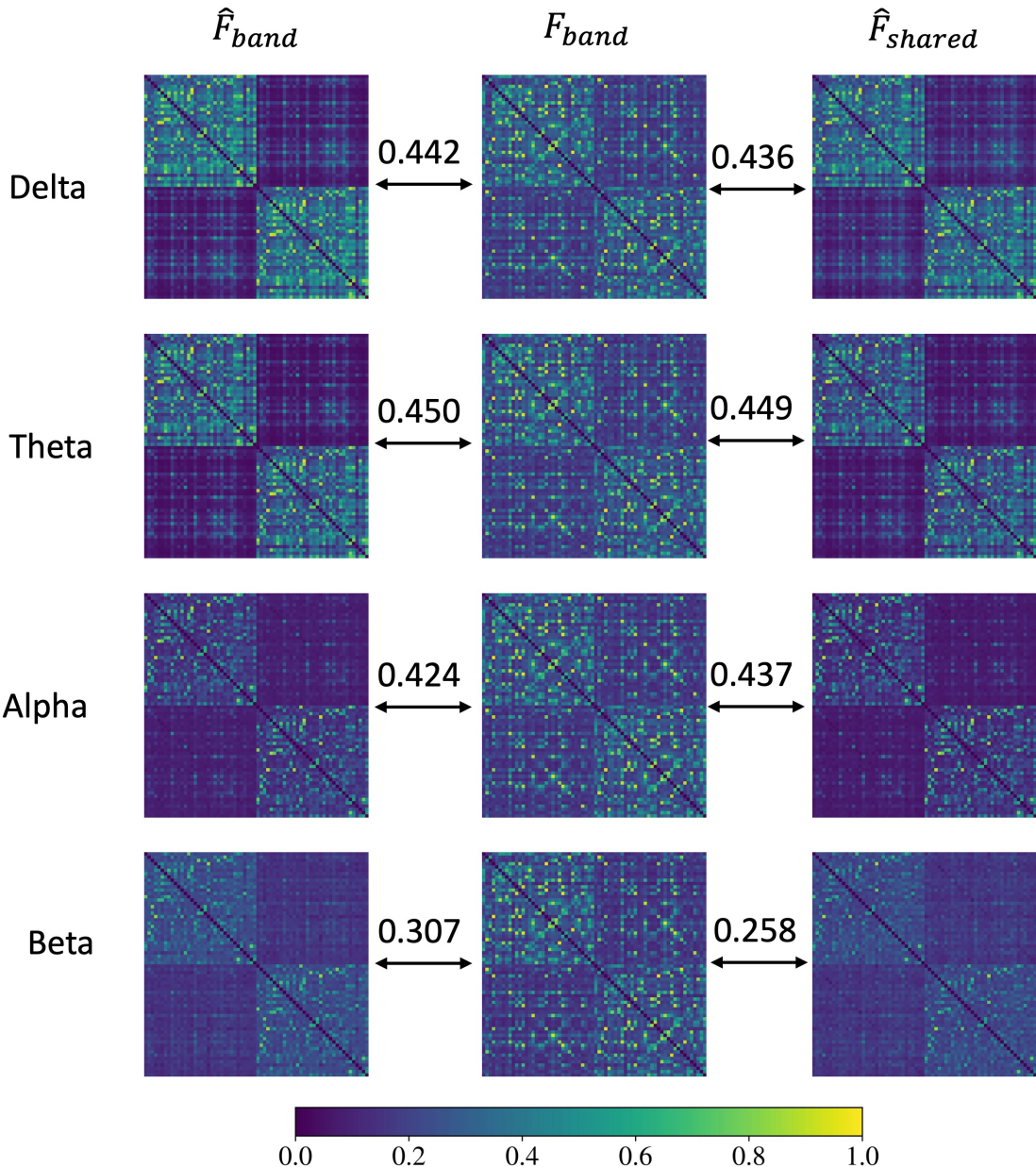


Figure 3: Left column: Mean estimated FCs for *delta*, *theta*, *alpha* and *beta* bands derived from band-specific SGM parameters (SGM-SBI), Middle column: Mean empirical FCs for *delta*, *theta*, *alpha* and *beta* bands across all subjects. Right column: Mean estimated FC for *delta*, *theta*, *alpha* and *beta* bands using band-shared SGM parameters (SGM-SBI-shared). The numbers above the arrows represent the average Pearson's correlation between estimated and empirical FCs.

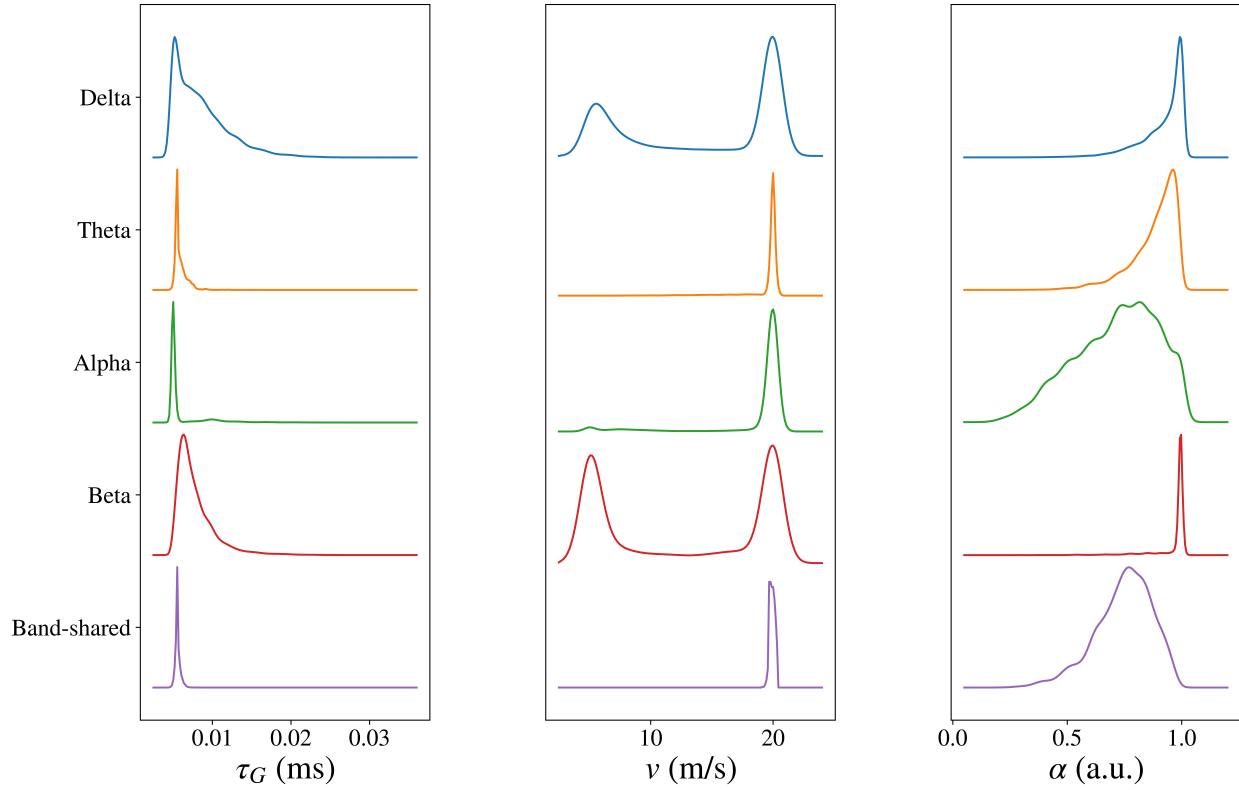


Figure 4: The posterior density plots of the SGM parameters estimated by fitting empirical FCs with SGM-SBI for *delta*, *theta*, *alpha*, *beta* bands and with SGM-SBI-shared method via stacking FCs from 4 bands together. The SGM parameters include graph time constant τ_g (left), transmission speed v (middle) and coupling constant α (right). Note that these density plots are based on data pooled from all 36 individuals. For better visualization, all the density curves are normalized such that they have the same peak value.

412 model-based fitting of MEG, that FC in all bands may be governed by the same biophysical process with
 413 the same characteristic parameters. The average Pearson's correlation between estimated and empirical FCs
 414 are displayed in Figure 3. FCs from band-specific and band-shared parameters have comparable Pearson's
 415 correlation with the empirical ones in *delta*, *theta* and *alpha* bands. However, in *beta* band, SGM-SBI
 416 performs notably better than SGM-SBI-shared.

417 4.6 Posterior distributions of fitted parameters

418 Now we showcase a key feature of the proposed SGM-SBI framework: its ability to produce the posterior
 419 distributions of SGM parameters. After the SBI-based fitting procedure on individual subjects, we draw 1000
 420 samples for each parameter and frequency band from every subject, pooling together the samples from all 36
 421 subjects. These posterior distributions are illustrated in Figure 4, where each subplot shows the univariate
 422 densities for each SGM parameter and all MEG bands. For enhanced visualization, each density curve is
 423 normalized to have the same peak value. Both versions of the model, SGM-SBI and SGM-SBI-shared, were
 424 fitted separately and are shown in the figure.

425 In the left column of Figure 4, the density plots of 4 band-specific and 1 band-shared results for the graph
426 time constant τ_g are displayed. Across all cases, the posterior distributions of τ_g exhibit a similar pattern with
427 a single peak around 0.005 ms. However, it's important to note that densities of τ_g from both *delta* and *beta*
428 bands show greater dispersion compared to others. The results of axonal conductance speed v are shown in
429 the middle column of Figure 4. The densities from *theta*, *alpha* bands and the band-shared results are all
430 single-peaked and concentrated around 20 m/s. In contrast, for the *delta* and *beta* bands, the distributions
431 display two distinct peaks situated around 5 and 20 m/s. The results for the global coupling constant α are
432 presented in the right column of Figure 4. When compared to densities for the time constant τ_g , those for α
433 exhibit a single peak situated approximately at 0.9 a.u., albeit with greater dispersion overall. The densities
434 derived from *delta* and *beta* bands demonstrate higher concentration than others. The band-shared results
435 appear to represent a consensus of the parameter posteriors across all bands – while this is to be expected, it
436 points to a possible disambiguating effect of the shared model compared to the fitting on individual bands.
437 We observe that the densities derived from band-shared results are closer to those from the *alpha* band across
438 all three SGM parameters, which indicates the importance of *alpha* band in the study of FC for MEG data.

439 In Figure 4, some of the density plots show double peaks. It is worth noting that the density plots are based
440 on data pooled from all 36 individuals. The double peaks in the density plots may be due to heterogeneity
441 amongst the subjects. To verify this, we plot the individual density plots for each subject and do not find
442 any double peaks in the density plots. We select two representative subjects and show the individual density
443 plots in Figure S1 and Figure S2. Another issue is that some of the density plots peak at the bounds of the
444 parameters. It raises the question, whether the bounds of the parameters in Table 1 are too tight. To investigate
445 this, we computed the average MSE across all subjects between the empirical FC and model-predicted FC
446 using the SGM-SBI method for different values of the parameters, well outside their prescribed bounds; these
447 are shown in Figure S4. We vary the one parameter and fix the other two parameters at their fitted values.
448 In the plot, the red dashed lines indicate the prescribed upper and lower bounds used during SBI inference.
449 The MSE plots show that the optimal values for each parameter are roughly within the prescribed lower and
450 upper bounds. Although the bounds are governed by biological constraints, the fact that the model fits are
451 generally contained within these bounds is reassuring.

452 4.7 Performance of SGM Graph Harmonic Model Fitting

453 We evaluate the performance of SGM-SBI model fitting in comparison to other methods such as connectome-
454 coupled NMM, eigen-mapping, and direct mapping (i.e. similarity between SC and FC). These alternative
455 models were chosen to represent a broad cross-section of recent efforts spanning a wide range of complexity
456 and computational burden. Coupled NMMs are the most complex and expensive, requiring very large
457 simulations, but are considered the most biologically accurate. A direct correlation between SC and FC is
458 clearly the fastest to evaluate and the least complex - while it does not represent any model, it serves as a
459 good baseline expectation of model-based approaches. In between the two extremes, we also evaluated the
460 eigen-mapping model, which captures the essential elements of diffusive spread of activity on structural
461 graphs [23, 44, 39], has a simple closed-form solution via graph harmonics, but does not give wideband
462 frequency response. There are several versions of the eigen-mapping method, each with varying number of
463 parameters. Here we chose one of the simplest, but the performance of alternative eigen models was quite
464 similar.

465 Detailed descriptions of these methods are available in Section 3.5 and performance metrics are outlined
466 in Section 3.4, which include MSE, Pearson's correlation and Lin's correlation. We derive FC from each
467 model, transform the vectorized FC matrix using the minmax operator, and then compute the metrics. These
468 metrics evaluate in different ways the models' ability to replicate empirical FCs.

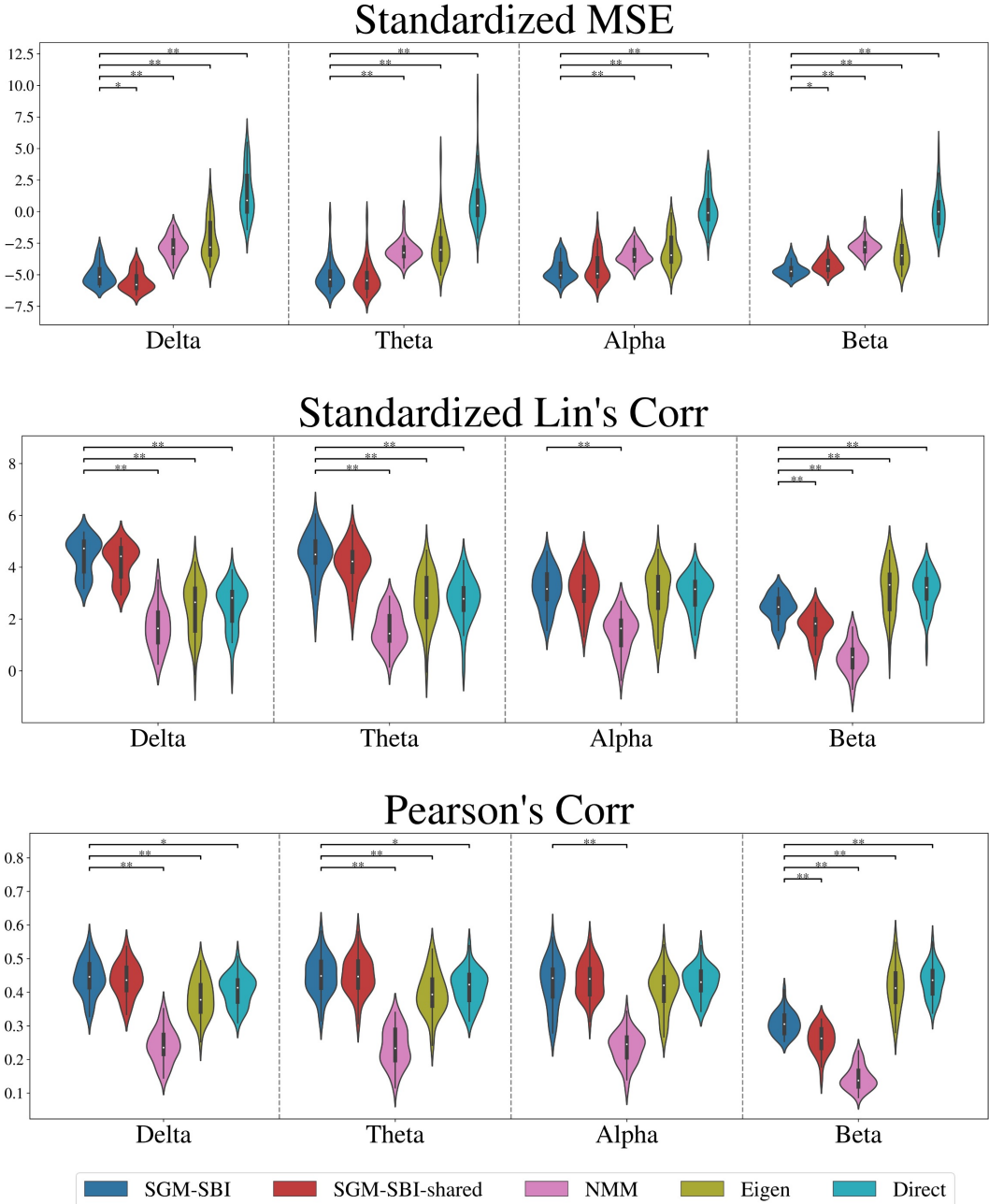


Figure 5: Violin plots of standardized MSE (top), standardized Lin's correlation (middle) and Pearson's correlation (bottom) between the empirical FC and model-predicted FC using five competing models: SGM-SBI, SGM-SBI-shared, NMM, eigen-mapping and direct mapping for *delta*, *theta*, *alpha* and *beta* bands. We aim to assess the performance of different methods on reproducing the empirical MEG FC matrices and use three metrics, MSE (the lower the better), Lin's correlation (the higher the better) and Pearson's correlation (the higher the better). Direct mapping refers to the simple correlation or MSE between SC and FC. We show the significant Student's t-test results comparing SGM-SBI with other methods. “*” indicates the test result with a p-value within [0.001, 0.05] and “**” indicates the test result with a p-value < 0.001.

469 Figure 5 presents the violin plots of MSE (top row), Lin’s correlation (middle row) and Pearson’s
470 correlation (bottom row) under SGM-SBI, SGM-SBI-shared, NMM, eigen-mapping and direct mapping. For
471 easier interpretation, we standardize the MSE and Lin’s correlation via subtracting the mean and dividing by
472 the standard deviation of the corresponding metrics from spinning the corresponding ROIs of the empirical
473 FCs on the brain surface. By doing so, we create a null model which preserves the spatial structure of the
474 FCs but randomizes the values [84]. We maintain Pearson’s correlation at the original scale as it has good
475 interpretation. The violin plots of raw MSE, Lin’s correlation and the standardized Pearson’s correlation
476 are shown in Figure S3 of the supplementary material. We conduct Student’s t-test comparing SGM-SBI
477 with other methods on these three metrics and present the significant results in Figure 5, “*” indicates the
478 test result with a p-value within [0.001, 0.05] and “**” indicates the test result with a p-value < 0.001. For
479 all three metrics, SGM-SBI is generally on par with SGM-SBI-shared in *delta*, *theta* and *alpha* bands
480 which is in agreement with the observation in Section 4.5. In terms of the MSE metric, the SGM-SBI-shared
481 shows some superiority while band-specific fitting performs better in correlation metrics. The distinction
482 between band-specific and band-shared fitting becomes more noticeable in the *beta* band where SGM-SBI
483 consistently surpasses SGM-SBI-shared across all metrics. Interestingly, the performance of SGM methods
484 decreases as the band frequency increases. This decline is particularly noticeable in the *beta* band, indicating
485 an inability of SGM to handle high-frequency bands. Taking Figures 3, 4 and 5 together, we note again
486 that the band-shared model gives roughly similar FC matrix, performance and parameter posteriors as the
487 band-specific models.

488 When compared to other methods, our method outperforms all others based on MSE metric across all
489 four bands. Regarding Lin’s correlation and Pearson’s correlation measures, our methods surpass others
490 in both *delta* and *theta* bands. In *alpha* band, SGM methods, eigen-mapping and direct mapping have
491 comparable Lin’s correlation and Pearson’s correlation while the NMM shows worst performance. In *beta*
492 band, two naive methods, i.e., eigen-mapping and direct mapping, exhibit highest correlations and SGM
493 methods still outperform NMM. The results show strong correlations but high MSE between empirical FCs
494 and SCs. This implies that while the SC can capture the overall changing trend in FC, it does not provide
495 valuable insights into the magnitude of FC. It is also possible that Pearson correlation may be less informative
496 as a performance metric than the other metrics, likely due to its insensitivity to scale.

497 **Execution time comparison.** In addition to visual resemblance and numerical performance of each
498 model, the execution time required to achieve those results is also a matter of high practical impact. We
499 therefore compare the computation time of two modelling methods, SGM-SBI and coupled NMM. In a
500 machine with Intel Xeon W-2255 CPU, SGM-SBI takes 119.119 seconds to fit the model to a single subject’s
501 MEG data, and 0.426 second to get 1000 samples on average for the *alpha* band. Using the same machine,
502 band, and subjects, the NMM model takes approximately an average of 1849.814 seconds to complete
503 fitting using the evolutionary algorithm and produce final results. The SGM-SBI is superior in terms of
504 computational efficiency compared with NMM. While 2 minutes per subject is not quite instantaneous, it is
505 in practice nearly so. The NMM simulations in contrast take around 30 minutes per subject - this is a vast
506 improvement over prior iterations of NMM methods, yet its execution time may not be considered practical
507 in some settings.

508 4.8 Performance of Model Fitting on Regional Level

509 We evaluate the performance of model fitting for SGM-SBI and SGM-SBI-shared at the regional level by
510 calculating the Pearson’s correlation between the corresponding columns of the empirical and estimated
511 FC matices. In Panel A of Figure 6, we display the mean Pearson’s correlation between the empirical and
512 estimated FCs for each ROI across all subjects in *delta*, *theta*, *alpha* and *beta* bands for both SGM-SBI

513 and SGM-SBI-shared. SGM-SBI and SGM-SBI-shared show similar patterns across all bands. In *delta*,
514 *theta* and *alpha* bands, the mean Pearson's correlation is above 0.5 for most ROIs while for *beta* band, the
515 mean Pearson's correlation is below 0.5 for most ROIs. Another observation is that across the brain, the
516 mean Pearson's correlation is higher in parietal and temporal lobes compared to other regions. We also
517 conduct the one-sample t-test versus 0 for the Pearson's correlation for each ROI and the negative log p-values
518 are shown in Panel B of Figure 6. To have a meaningful test, we standardize the Pearson's correlation via
519 subtracting the mean and dividing by the standard deviation of the Pearson's correlation from spinning the
520 corresponding ROIs of the empirical FCs on the brain surface as we do in Section 4.5. The cutoff value
521 is set to $-\log(0.05/68) \approx 7.2$ after Bonferroni correction and only significant results are shown. In *delta*,
522 *theta* and *alpha* bands, most of the ROIs have significant Pearson's correlation while for *beta* band, most of
523 significant ROIs are located in the parietal and temporal lobes.

524 4.9 Individual Level Results

525 We select two representative subjects to show the individual-level results. Specifically, we choose the subjects
526 with the Pearson's correlation between the empirical FC and model-predicted (SGM-SBI model) FC closest
527 to the mean of all subjects on *alpha* band. The results are shown in Figure S1 and Figure S2.

528 For both subjects, the real part of first three complex Laplacian eigenvectors in the *alpha* band (Panel
529 A of Figure S1 and Figure S2) are very similar to the mean eigenvectors across all subjects (Figure 2A).
530 The estimated FCs from two subjects are also consistent with the mean estimated FCs across all subjects
531 (Figure 3). In term of the posterior distributions of the SGM parameters, the group-level results show some
532 bi-modal distributions for transmission speed v in *delta* and *beta* bands (Figure 4). In the individual-level
533 results, the posterior distributions only show a single peak for all three SGM parameters in all bands (Panel
534 B of Figure S1 and Figure S2). Though, the peak locations for the transmission speed v in *delta* and *beta*
535 bands are different between the two subjects.

536 5 Discussion

537 5.1 Summary and significance of key findings

538 In this work, we advance the emerging concept of structural connectome (SC) graph harmonics in the brain
539 by imbuing them with biophysical mechanisms and by demonstrating that a parsimonious combination of
540 harmonics is capable of recapitulating frequency-band-specific FC of MEG recordings. The study fills a
541 critical gap in the field, wherein harmonics have been shown to possess predictive power for capturing FC but
542 have not been shown to possess biophysical meaning, while biophysically-driven computational models do not
543 have direct involvement of graph harmonics. Our goal was to combine both the elegance of graph harmonics
544 and the biophysical relevance of detailed NMMs. We achieved this goal via a biophysical linearized model
545 of the propagation of brain activity on SC, leveraging and extending advances in modeling wideband MEG
546 power spectra using graph eigenspectra [61, 9]. We provided for the first time a fully frequency-resolved
547 description of FC, at any arbitrary frequency. This description is direct and does not require either simulations
548 in time or indirect calculation of FC via the narrow-band Hilbert envelope [56, 68].

549 The resulting graph model has only 3 global and invariant parameters, each with a well understood
550 biological meaning: characteristic time scale of long-range projection neurons τ_G (unit: ms); axonal
551 conductance speed v (m/s); and the connectome coupling constant α (unitless). It is therefore noteworthy
552 that empirical FC, which has a prominent spatial organization, can be successfully predicted by a model
553 consisting of only 3 spatially invariant parameters. The implication is that spatial variance of FC is directly a

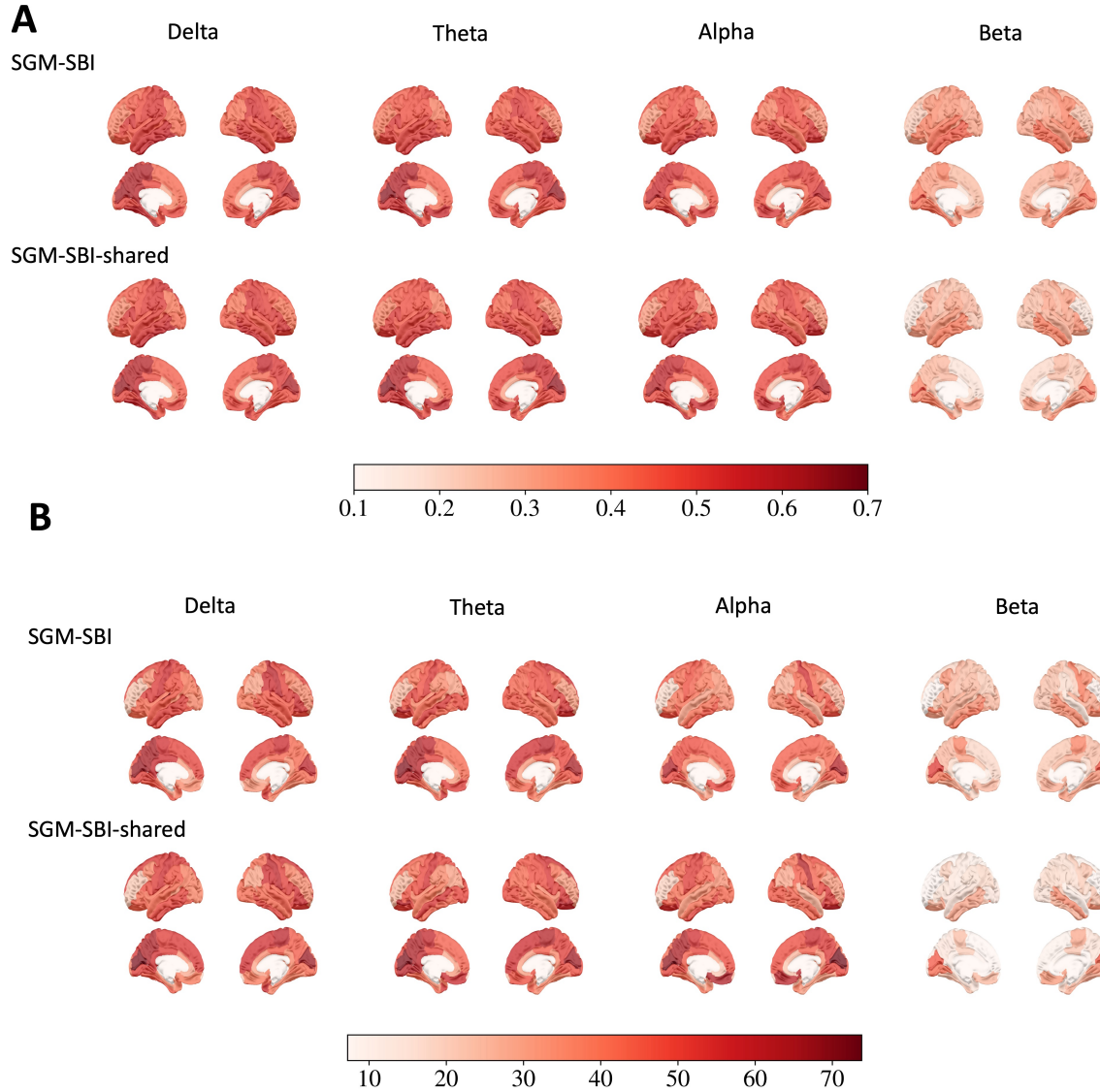


Figure 6: The results of the regional level evaluation for SGM-SBI and SGM-SBI-shared. **A:** The mean Pearson’s correlation between the empirical and estimated FCs for each ROI across all subjects in *delta*, *theta*, *alpha* and *beta* bands. **B:** The negative log p-values of the one-sample t-test versus 0 for the Pearson’s correlation for each ROI across all subjects in *delta*, *theta*, *alpha* and *beta* bands. The cutoff value is set to $-\log(0.05/68) \approx 7.2$ after Bonferroni correction and only significant results are shown.

consequence of the spatial distribution of the low graph harmonics of SC. Note that local model parameters, which were critical in prior fitting of SGM to wideband spectra, are effectively removed in the current context following normalization of the SGM covariance matrix by its diagonal. This makes intuitive sense, since local processes may affect local spectral power but not long range synchrony between distant regions.

In order to convert these theoretical advances into a practical tool we designed a speedy and flexible deep learning network for inferring the biophysical parameters. After the network has been trained on sufficient simulation-based training samples, it could achieve model parameter inference almost instantaneously for a given subject. Parameter inference has historically been an intractable challenge in neural system modeling, and prior coupled NMMs require a combination of hand-tuning and grid search [62, 63]. In contrast, we were not only able to obtain best-fit biophysical parameters very quickly (within seconds) but also to give their full posterior distributions and accompanying confidence bounds. We demonstrated this inference ability, critical for potential practical applications of model-based SC-FC inference, on a study of 36 healthy individual subjects' MEG recordings. With the analytical frequency-resolved description of FC, parameter inference is substantially faster and requires limited memory for model computations. By incorporating the SBI framework for inferring parameters, obtaining the posterior densities of parameters is tractable. This resolves a key intractable challenge inherent in the inference of current coupled NMMs, which require lengthy and massive numerical simulations, and opens the door to future practical applications of model fitting to MEG data. Remarkably, using only the 3 biophysical parameters and only a few (3-5) graph harmonics, the model is able to reproduce empirical MEG FC in all frequency bands of interest, quantifiably better than all competing benchmark methods we tested. The trained DL-based SBI network gives full posterior distributions and confidence bounds, which are necessary for applications where a measure of uncertainty is helpful.

Finally, we explored an important issue in prior modeling studies on MEG: would the model parameters be frequency-band-specific, or global for a given subject? Most prior successes in theoretical fitting of MEG data appear to be band-specific, implying very different biophysical properties in different bands. This is long understood to be biologically implausible, since the parameters pertain to biological systems and should not vary across frequencies. The emergence of the correct frequency dependency should be a key test of a successful computational neural model, a test that is rarely passed in existing literature. Our demonstration that a single parametrization of the harmonic model, i.e. a unique combination of parameters τ_G, v, α , is capable of reproducing MEG FC in all frequency bands of interest, gives renewed assurance that our computational model passes this test of plausibility. Indeed, we were able to show that the band-shared model achieved similar FC matrix visualization (Figure 3), parameter posteriors (Figure 4) and numerical performance metrics (Figure 5) when compared to SGM models fitted to each frequency band separately. If anything, the shared model showed evidence of superior disambiguation and consensus amongst bands.

5.2 Proposed model is tractable compared to coupled neural mass simulations

We numerically compared (Figure 5) the proposed SGM-SBI model with a current and open-source implementation of NMM simulations. Across all results we evaluated, the connectome-coupled NMM was consistently one of the least accurate predictors of FC in all bands. This might appear surprising at first, given the deep and wide popularity of NMMs in the field, their long history and their ability to accommodate biological processes of high complexity. It is therefore useful to understand the issues that might impact the accuracy and inference performance of these methods.

While coupled NMMs have been widely used to capture MEG FC, they suffer from some challenges that can make robust inference of model parameters intractable, discussed in detail previously [49, 62]. First, NMMs simulations take a long time and compute power since they require numerical integration

598 of coupled differential equations. Second, since these non-linear model solutions can be vastly different
599 depending on the parameter regime, certain model parameters are hand-tuned to be near a bifurcation point
600 and only the remaining parameters are optimized for by fitting to the empirical data, typically using a
601 grid search optimization [85, 60]. Lastly, most prior NMMs studies have focused on fitting to group-level
602 FC [67, 86, 56, 87] with fewer studies focused on fitting to individual-level FC [88–90]. SGM is able
603 to address all of these challenges given its analytic closed-form solution consisting of only a few global
604 parameters, and its ability to fit to individual-level FC fast with the SBI framework, taking 2 minutes compared
605 to 30 minutes by NMM.

606 A key point to note is that most neural mass models are non-linear and can therefore exhibit a rich
607 dynamical repertoire in their oscillatory behavior [56, 59, 58]. Such behaviors are quantified in terms of
608 bifurcations defining solution regimes that are quantified by fixed points, limit cycles, and chaotic behavior.
609 Since the current graph model is linear, it can only exhibit stable or oscillatory, but no chaotic behavior [91].
610 It is still an open question whether such non-linearities are required to capture macroscopic structure-function
611 relationships. Indeed, macroscopic spatial and frequency patterns are largely identical across individuals [92–
612 94]. It has been suggested that emergent long-range activity can be independent of microscopic local activity
613 of individual neurons [95, 92, 52, 23, 13, 48], and that these long-range activities may be regulated by the
614 long-range connectivity [96, 97, 86, 98]. In addition, linear models outperformed non-linear models in
615 predicting resting-state fMRI time series [99]. Therefore, to capture macroscopic phenomena, the present
616 deterministic graph model may be sufficient, with the additional advantage of tractable model inference.

617 5.3 Alternative inference methods

618 In prior studies that use a similar spectral graph model (SGM) [9, 61, 49, 91], annealing-based optimization
619 was used for inference, which suffers from two limitations. First, it can only provide a single point estimate
620 of the parameters. In a neural model like SGM, it is desirable to find out not only the best, but all parameter
621 settings, compatible with the observed data. The variability of the parameters under the observation can
622 provide more insights about the neural models and processes [75, 100]. Annealing optimization fails to
623 meet this requirement. Moreover, it is difficult to incorporate prior knowledge about neural processes with
624 annealing, which further limits its application. The free parameters in neural models typically relate to
625 biological processes, hence their inference must utilize constraints that avoid unreasonable solutions. Using
626 prior knowledge of these biological quantities can not only increase optimization efficiency but also make
627 them more robust.

628 It is also possible to use Markov chain Monte Carlo (MCMC) methods [101] to conduct Bayesian
629 inference, as our model has a closed-form solution in the Fourier frequency domain. However, the posterior
630 densities are challenging to analyze, a long burn-in step is required for MCMC methods to reach the
631 equilibrium distribution, and samples from the equilibrium distribution are correlated. Thus sampling from
632 MCMC can be time-consuming for SGM. Previously, an MCMC-based inference was unable to capture the
633 spectral features using a nonlinear neural mass model [62]. In comparison, SBI is more flexible and can
634 handle complicated likelihood functions. More importantly, SBI is trained upfront with simulation samples,
635 which helps to reduce the requirements of real data and greatly improves inference speed.

636 Dynamic causal modeling (DCM) [64, 65] is a Bayesian approach for estimating and comparing models
637 of functional signals (e.g. fMRI, MEG, or EEG time series). The activities of neuronal populations are
638 modeled by systems of differential equations representing synaptic coupling and its plasticity. The ‘hidden’
639 neuronal dynamics are linked to measured time series data through a biologically grounded forward model.
640 Recent work on regression DCM [102, 103] proposes local neural mass models formulated in the steady state
641 frequency domain, with the effective connectivity evaluated from the cross spectra. Such models assume

642 numerous degrees of freedom, while the present SGM model requires only three global parameters. Hence
643 there is a key difference in the goals and outcomes of DCM and the present study: the former seeks to
644 estimate the entire matrix of pairwise associations from the time series data, whereas the latter seeks to
645 enforce SC as the basis for predicting FC. Another important difference between DCM and SGM is that
646 DCM requires variational Bayesian inference, whereas here we leveraged the SBI tool for posterior inference
647 of the global SGM parameters with ranges based on underlying biophysics.

648 5.4 Limitations

649 In this work FC was constructed using absolute coherence, while other groups have favored partial coherence
650 instead [30]. While we enforced spatial uniformity in model parameters, it is possible that some spatial
651 heterogeneity may help improve model fits – an aspect we will explore in the future. Specifically, it might be
652 necessary to accommodate the variation of the speed parameter as a function of the amount of myelination
653 and synaptic strength in different regions. Various methodological limitations are relevant here. Our structural
654 connectivity network was obtained based on diffusion-weighted images which are only an approximation of
655 white-matter axonal connections. The MEG functional network was source-reconstructed using a minimum-
656 variance adaptive beamformer, a process which may be ill-posed and one that has difficulty in estimating
657 deep brain sources [104, 105]. Despite these approximations, macroscopic spatial and frequency patterns
658 are largely robust across individuals [92–94]. We have discussed these in detail in prior works [27, 49]. Our
659 model’s FC output is directly comparable to coherence-based FC, due to the connection with cross-spectral
660 density. The relevance of our model in producing other types of FC, e.g. amplitude envelope correlation, is
661 unclear at this time, and will be explored in future work.

662 Another limitation is the assumption, noted in Section 2.2, that the *the driving input signal is uncorre-*
663 *lated across regions and across time*. We assume for simplicity that $\mathcal{E}(\mathbf{P}(\omega)\mathbf{P}(\omega)^H)$ has independent and
664 identically distributed white spatial and temporal covariance structure. This assumption greatly simplifies
665 the mathematics and the final expression for the model-predicted spatial covariance. However, in some
666 instances, even at rest, the driving function may have a specific spatial covariance structure, such as those
667 related to thalamocortical drive or correlated sensory or motor signals. We plan to explore the influence of
668 such spatial covariance structures in future work. In contrast, temporal covariance in the driving function
669 will only result in frequency-specific scaling of the model covariance, altering predictions but not the overall
670 model architecture.

671 Furthermore, our model and empirical FC calculations do not consider the role of spatial leakage which is
672 considered a major confound in MEG FC measures, especially at voxel level imaging. Incorporating spatial
673 leakage in model FC calculations to match with empirical FC that account for spatial leakage is something
674 we will pursue in the future.

675 5.5 Potential applications

676 Given the ease of parameter inference, this work can be readily extended to investigate biophysical alterations
677 resulting in abnormal FC in diseases, such as in Alzheimer’s disease [106–109], epilepsy [110], addiction
678 [111], and multiple sclerosis [112], to name a few. It can also be used to examine underlying biophysical
679 mechanisms that shape FC in processes such as cognition [113]. Since the proposed graph model parameters
680 have biophysical interpretability, inferring them can suggest meaningful biophysical alterations in the excitatory
681 and inhibitory neuronal populations that can result in changes in FC. Previously, we have shown such
682 alterations at a local level in Alzheimer’s disease by investigating the empirical MEG spectra [114]. Inferring
683 such biophysical mechanisms is unfeasible with examining raw neuroimaging data alone, or with models

684 where parameter inference is intractable. Additionally, the posterior densities of model parameters provide us
685 with error bounds that can be useful for clinical applications, specifically for identifying biophysical markers
686 of disease. In the future, we will also aim at simultaneously capturing both FC and power spectra using graph
687 harmonics, e.g. [61]. This will aid in identifying common underlying biophysical mechanisms that shape
688 both spectra as well as FC.

Data and Code Availability

The code and processed datasets for this work can be found in this github repository: https://github.com/JINhuaqing/SBI-SGM-FC_paper.

Author Contributions

F.A. and R.A.conceived the study; H.J. and F.A. preprocessed the data; H.J. conducted all analyses; B.S.S., N.S.S and R.A. consulted on the analyses; H.J., F.A., P.V., and R.A. wrote the first draft of the manuscript; and H.J., N.S.S. and R.A. contributed to the manuscript writing and final manuscript approval.

Declaration of Competing Interest

The authors have no conflicts to report.

Acknowledgments

This work was supported by NIH grants K25AG071840, R01NS132766.

References

- [1] Alex Fornito, Andrew Zalesky, and Michael Breakspear. The connectomics of brain disorders. *Nature Reviews Neuroscience*, 16(3):159–172, 2015.
- [2] Laura E. Suárez, Ross D. Markello, Richard F. Betzel, and Bratislav Misic. Linking structure and function in macroscale brain networks. *Trends in Cognitive Sciences*, 24(4):302–315, 2020.
- [3] Ruxandra I Tivadar and Micah M Murray. A primer on electroencephalography and event-related potentials for organizational neuroscience. *Organizational Research Methods*, 22(1):69–94, 2019.
- [4] Fernando Lopes da Silva. Eeg and meg: relevance to neuroscience. *Neuron*, 80(5):1112–1128, 2013.
- [5] Ed Bullmore and Olaf Sporns. Complex brain networks: graph theoretical analysis of structural and functional systems. *Nature Reviews Neuroscience*, 10(3):186–198, 2009.
- [6] Danielle S Bassett and Edward T Bullmore. Human brain networks in health and disease. *Current Opinion in Neurology*, 22(4):340, 2009.

- [7] Matthew J. Brookes, Joanne R. Hale, Johanna M. Zumer, Claire M. Stevenson, Susan T. Francis, Gareth R. Barnes, Julia P. Owen, Peter G. Morris, and Srikantan S. Nagarajan. Measuring functional connectivity using meg: Methodology and comparison with fcmri. *NeuroImage*, 56(3):1082–1104, 2011.
- [8] M.J. Brookes, M.W. Woolrich, and G.R. Barnes. Measuring functional connectivity in meg: A multivariate approach insensitive to linear source leakage. *NeuroImage*, 63(2):910–920, 2012.
- [9] Parul Verma, Srikantan Nagarajan, and Ashish Raj. Spectral graph theory of brain oscillations—revisited and improved. *NeuroImage*, 249:118919, 2022.
- [10] Patric Hagmann, Leila Cammoun, Xavier Gigandet, Reto Meuli, Christopher J Honey, Van J Wedeen, and Olaf Sporns. Mapping the structural core of human cerebral cortex. *PLOS Biology*, 6(7):1–15, 07 2008.
- [11] Mikail Rubinov and Olaf Sporns. Complex network measures of brain connectivity: uses and interpretations. *NeuroImage*, 52(3):1059–1069, 2010.
- [12] Bratislav Mišić, Richard F Betzel, Marcel A De Reus, Martijn P Van Den Heuvel, Marc G Berman, Anthony R McIntosh, and Olaf Sporns. Network-level structure-function relationships in human neocortex. *Cerebral Cortex*, 26(7):3285–3296, 2016.
- [13] Bratislav Mišić, Olaf Sporns, and Anthony R McIntosh. Communication efficiency and congestion of signal traffic in large-scale brain networks. *PLoS Comput Biol*, 10(1):e1003427, 2014.
- [14] Steven H Strogatz. Exploring complex networks. *Nature*, 410(6825):268–276, 2001.
- [15] Randy L. Buckner, Abraham Z. Snyder, Benjamin J. Shannon, Gina LaRossa, Rimmon Sachs, Anthony F. Fotenos, Yvette I. Sheline, William E. Klunk, Chester A. Mathis, John C. Morris, and Mark A. Mintun. Molecular, structural, and functional characterization of alzheimer’s disease: Evidence for a relationship between default activity, amyloid, and memory. *Journal of Neuroscience*, 25(34):7709–7717, 2005.
- [16] Sophie Achard, Raymond Salvador, Brandon Whitcher, John Suckling, and Ed Bullmore. A Resilient, Low-Frequency, Small-World Human Brain Functional Network with Highly Connected Association Cortical Hubs. *Journal of Neuroscience*, 26(1):63–72, 2006.
- [17] Danielle Smith Bassett and Ed Bullmore. Small-world brain networks. *The Neuroscientist*, 12(6):512–523, 2006. PMID: 17079517.
- [18] Nivedita Chatterjee and Sitabhra Sinha. Understanding the mind of a worm: hierarchical network structure underlying nervous system function in *c. elegans*. In Rahul Banerjee and Bikas K. Chakrabarti, editors, *Models of Brain and Mind*, volume 168 of *Progress in Brain Research*, pages 145–153. Elsevier, 2007.
- [19] Yong He, Zhang Chen, and Alan Evans. Structural insights into aberrant topological patterns of large-scale cortical networks in alzheimer’s disease. *Journal of Neuroscience*, 28(18):4756–4766, 2008.
- [20] A Ghosh, Y Rho, AR McIntosh, R Kötter, and VK Jirsa. Cortical network dynamics with time delays reveals functional connectivity in the resting brain. *Cognitive Neurodynamics*, 2(2):115–120, 2008.

- [21] Mikail Rubinov, Olaf Sporns, Cees van Leeuwen, and Michael Breakspear. Symbiotic relationship between brain structure and dynamics. *BMC Neuroscience*, 10(1):1–18, 2009.
- [22] Martijn P. van den Heuvel, René C.W. Mandl, René S. Kahn, and Hilleke E. Hulshoff Pol. Functionally linked resting-state networks reflect the underlying structural connectivity architecture of the human brain. *Human Brain Mapping*, 30(10):3127–3141, 2009.
- [23] Farras Abduelnoor, Henning U. Voss, and Ashish Raj. Network diffusion accurately models the relationship between structural and functional brain connectivity networks. *NeuroImage*, 90:335–347, 2014.
- [24] Ann M Hermundstad, Danielle S Bassett, Kevin S Brown, Elissa M Aminoff, David Clewett, Scott Freeman, Amy Frithsen, Arianne Johnson, Christine M Tipper, Michael B Miller, et al. Structural foundations of resting-state and task-based functional connectivity in the human brain. *Proceedings of the National Academy of Sciences*, 110(15):6169–6174, 2013.
- [25] Hae-Jeong Park and Karl Friston. Structural and functional brain networks: from connections to cognition. *Science*, 342(6158), 2013.
- [26] Farras Abduelnoor, Michael Dayan, Orrin Devinsky, Thomas Thesen, and Ashish Raj. Functional brain connectivity is predictable from anatomic network’s Laplacian eigen-structure. *NeuroImage*, 172:728–739, 2018.
- [27] Xie, Chang Cai, Pablo F. Damasceno, Srikantan S. Nagarajan, and Ashish Raj. Emergence of canonical functional networks from the structural connectome. *NeuroImage*, 237:118190, 2021.
- [28] Sanjay Ghosh, Ashish Raj, and Srikantan S. Nagarajan. A joint subspace mapping between structural and functional brain connectomes. *NeuroImage*, 272:119975, 2023.
- [29] Eirini Messaritaki, Sonya Foley, Simona Schiavi, Lorenzo Magazzini, Bethany Routley, Derek K Jones, and Krish D Singh. Predicting meg resting-state functional connectivity from microstructural information. *Network Neuroscience*, 5(2):477–504, 2021.
- [30] Anirudh Wodeyar and Ramesh Srinivasan. Structural connectome constrained graphical lasso for MEG partial coherence. *Network Neuroscience*, 6(4):1219–1242, 10 2022.
- [31] Andrew Ng, Michael Jordan, and Yair Weiss. On spectral clustering: Analysis and an algorithm. *Advances in Neural Information Processing Systems*, 14:849–856, 2001.
- [32] Risi Imre Kondor and John Lafferty. Diffusion kernels on graphs and other discrete structures. In *Proceedings of the 19th international conference on machine learning*, volume 2002, pages 315–322, 2002.
- [33] Rasmus Larsen, Mads Nielsen, and Jon Sporring. *Medical Image Computing and Computer-Assisted Intervention–MICCAI 2006: 9th International Conference, Copenhagen, Denmark, October 1–6, 2006, Proceedings, Part I*, volume 4190. Springer, 2006.
- [34] Benjamin Auffarth. Spectral graph clustering. *Universitat de Barcelona, course report for Technicas Avanzadas de Aprendizaj, at Universitat Politecnica de Catalunya*, 2007.

- [35] Selen Atasoy, Isaac Donnelly, and Joel Pearson. Human brain networks function in connectome-specific harmonic waves. *Nature Communications*, 7:10340, 2016.
- [36] P. A. Robinson, X. Zhao, K. M. Aquino, J. D. Griffiths, S. Sarkar, and Grishma Mehta-Pandejee. Eigenmodes of brain activity: Neural field theory predictions and comparison with experiment. *NeuroImage*, 142:79–98, 2016.
- [37] James C Pang, Kevin M Aquino, Marianne Oldehinkel, Peter A Robinson, Ben D Fulcher, Michael Breakspear, and Alex Fornito. Geometric constraints on human brain function. *Nature*, 618(7965):566–574, 2023.
- [38] Fan RK Chung. *Spectral graph theory*, volume 92. American Mathematical Soc., 1997.
- [39] Samuel Deslauriers-Gauthier, M Zucchelli, M Frigo, and Rachid Deriche. A unified framework for multimodal structure-function mapping based on eigenmodes. *Medical Image Analysis*, 66:101799, 2020.
- [40] Jil Meier, Prejaas Tewarie, Arjan Hillebrand, Linda Douw, Bob W. van Dijk, Steven M. Stufflebeam, and Piet Van Mieghem. A Mapping Between Structural and Functional Brain Networks. *Brain Connectivity*, 6(4):298–311, 2016.
- [41] Cassiano Becker, Sérgio Pequito, George Pappas, Michael Miller, Scott Grafton, Danielle Bassett, and Victor M. Preciado. Spectral mapping of brain functional connectivity from diffusion imaging. *Nature Scientific Reports*, 8(1411):1–15, 2018.
- [42] Prejaas Tewarie, B Prasse, JM Meier, F Santos, L Douw, MM Schoonheim, CJ Stam, P 5 Van Mieghem, and A Hillebrand. Mapping functional brain networks from the structural connectome: Relating the series expansion and eigenmode approaches. *NeuroImage*, 216:116805, 2020.
- [43] Giulia Lioi, Vincent Gripon, Abdelbasset Brahim, François Rousseau, and Nicolas Farrugia. Gradients of connectivity as graph fourier bases of brain activity. *Network Neuroscience*, 5(2):322–336, 2021.
- [44] Farras Abdnour, Michael Dayan, Orrin Devinsky, Thomas Thesen, and Ashish Raj. Algebraic relationship between the structural network’s Laplacian and functional network’s adjacency matrix is preserved in temporal lobe epilepsy subjects. *NeuroImage*, 228:117705, 2021.
- [45] Maria Giulia Preti and Dimitri Van De Ville. Decoupling of brain function from structure reveals regional behavioral specialization in humans. *Nature Communications*, 10, 2019.
- [46] Joan Rué-Queralt, Valentina Mancini, Vincent Rochas, Caren Latrèche, Peter J Uhlhaas, Christoph M Michel, Gijs Plomp, Stephan Eliez, and Patric Hagmann. The coupling between the spatial and temporal scales of neural processes revealed by a joint time-vertex connectome spectral analysis. *NeuroImage*, 280:120337, 2023.
- [47] Katharina Glomb, Joan Rue Queralt, David Pascucci, Michaël Defferrard, Sébastien Tourbier, Margherita Carboni, Maria Rubega, Serge Vulliemoz, Gijs Plomp, and Patric Hagmann. Connectome spectral analysis to track EEG task dynamics on a subsecond scale. *NeuroImage*, page 117137, 2020.
- [48] Bratislav Mišić, Richard F Betzel, Azadeh Nematzadeh, Joaquin Goni, Alessandra Griffa, Patric Hagmann, Alessandro Flammini, Yong-Yeol Ahn, and Olaf Sporns. Cooperative and competitive spreading dynamics on the human connectome. *Neuron*, 86(6):1518–1529, 2015.

- [49] Ashish Raj, Parul Verma, and Srikanth Nagarajan. Structure-function models of temporal, spatial, and spectral characteristics of non-invasive whole brain functional imaging. *Frontiers in Neuroscience*, 16:959557–959557, 2022.
- [50] Hugh R Wilson and Jack D Cowan. A mathematical theory of the functional dynamics of cortical and thalamic nervous tissue. *Kybernetik*, 13(2):55–80, 1973.
- [51] Olivier David and Karl J. Friston. A neural mass model for MEG/EEG:: coupling and neuronal dynamics. *NeuroImage*, 20(3):1743–1755, 2003.
- [52] Alain Destexhe and Terrence J Sejnowski. The Wilson–Cowan model, 36 years later. *Biological Cybernetics*, 101(1):1–2, 2009.
- [53] Sami El Boustani and Alain Destexhe. A master equation formalism for macroscopic modeling of asynchronous irregular activity states. *Neural Computation*, 21(1):46–100, 2009.
- [54] C. J. Honey, O. Sporns, L. Cammoun, X. Gigandet, J. P. Thiran, R. Meuli, and P. Hagmann. Predicting human resting-state functional connectivity from structural connectivity. *Proceedings of the National Academy of Sciences*, 106(6):2035–2040, 2009.
- [55] A. Spiegler and V. Jirsa. Systematic approximations of neural fields through networks of neural masses in the virtual brain. *NeuroImage*, 83:704–725, 2013.
- [56] Joana Cabral, Morten L. Kringelbach, and Gustavo Deco. Exploring the network dynamics underlying brain activity during rest. *Progress in Neurobiology*, 114:102–131, 2014.
- [57] Sarah Feldt Muldoon, Fabio Pasqualetti, Shi Gu, Matthew Cieslak, Scott T. Grafton, Jean M. Vettel, and Danielle S. Bassett. Stimulation-Based Control of Dynamic Brain Networks. *PLOS Computational Biology*, 12(9):1–23, 09 2016.
- [58] Constantinos Siettos and Jens Starke. Multiscale modeling of brain dynamics: from single neurons and networks to mathematical tools. *WIREs Systems Biology and Medicine*, 8(5):438–458, 2016.
- [59] Joana Cabral, Morten L. Kringelbach, and Gustavo Deco. Functional connectivity dynamically evolves on multiple time-scales over a static structural connectome: Models and mechanisms. *NeuroImage*, 160:84–96, 2017. Functional Architecture of the Brain.
- [60] Michael Breakspear. Dynamic models of large-scale brain activity. *Nature Neuroscience*, 20(3):340–352, 2017.
- [61] Ashish Raj, Chang Cai, Xihe Xie, Eva Palacios, Julia Owen, Pratik Mukherjee, and Srikanth Nagarajan. Spectral graph theory of brain oscillations. *Human Brain Mapping*, 41(11):2980–2998, 2020.
- [62] Xihe Xie, Amy Kuceyeski, Sudhin A Shah, Nicholas D Schiff, SS Nagarajan, and Ashish Raj. Parameter identifiability and non-uniqueness in connectome based neural mass models. *bioRxiv*, page 480012, 2019.
- [63] Katharina Glomb, Joana Cabral, Anna Cattani, Alberto Mazzoni, Ashish Raj, and Benedetta Franceschiello. Computational models in electroencephalography. *Brain topography*, pages 1–20, 2021.

- [64] Stefan J Kiebel, Marta I Garrido, Rosalyn J Moran, and Karl J Friston. Dynamic causal modelling for eeg and meg. *Cognitive Neurodynamics*, 2(2):121, 2008.
- [65] Dimitris A Pinotsis, Rosalyn J Moran, and Karl J Friston. Dynamic causal modeling with neural fields. *NeuroImage*, 59(2):1261–1274, 2012.
- [66] Agus Hartoyo, Peter J. Cadusch, David T. J. Liley, and Damien G. Hicks. Parameter estimation and identifiability in a neural population model for electro-cortical activity. *PLOS Computational Biology*, 15(5):1–27, 05 2019.
- [67] Prejaas Tewarie, Romesh Abeysuriya, Aine Byrne, George C. O’Neill, Stamatios N. Sotiroopoulos, Matthew J. Brookes, and Stephen Coombes. How do spatially distinct frequency specific MEG networks emerge from one underlying structural connectome? the role of the structural eigenmodes. *NeuroImage*, 186:211–220, 2019.
- [68] Prejaas Tewarie, Bastian Prasse, Jil Meier, Kanad Mandke, Shaun Warrington, Cornelis J Stam, Matthew J Brookes, Piet Van Mieghem, Stamatios N Sotiroopoulos, and Arjan Hillebrand. Predicting time-resolved electrophysiological brain networks from structural eigenmodes. *Human Brain Mapping*, 2022.
- [69] Xi He Xie, Megan Stanley, and Pablo F. Damasceno. Raj-Lab-UCSF/spectrome: Spectral Graph Model of Neural Dynamics on Connectomes, January 2020.
- [70] Rahul S Desikan, Florent Ségonne, Bruce Fischl, Brian T Quinn, Bradford C Dickerson, Deborah Blacker, Randy L Buckner, Anders M Dale, R Paul Maguire, Bradley T Hyman, et al. An automated labeling system for subdividing the human cerebral cortex on MRI scans into gyral based regions of interest. *NeuroImage*, 31(3):968–980, 2006.
- [71] Huaqing Jin, Parul Verma, Fei Jiang, Srikanth Nagarajan, and Ashish Raj. Bayesian inference of a spectral graph model for brain oscillations. *bioRxiv*, pages 2023–03, 2023.
- [72] Alexandre Gramfort, Martin Luessi, Eric Larson, Denis A. Engemann, Daniel Strohmeier, Christian Brodbeck, Roman Goj, Mainak Jas, Teon Brooks, Lauri Parkkonen, and Matti S. Hämäläinen. MEG and EEG data analysis with MNE-Python. *Frontiers in Neuroscience*, 7(267):1–13, 2013.
- [73] Alexandre Gramfort, Martin Luessi, Eric Larson, Denis A Engemann, Daniel Strohmeier, Christian Brodbeck, Roman Goj, Mainak Jas, Teon Brooks, Lauri Parkkonen, et al. Meg and eeg data analysis with mne-python. *Frontiers in neuroscience*, page 267, 2013.
- [74] Alvaro Tejero-Cantero, Jan Boelts, Michael Deistler, Jan-Matthis Lueckmann, Conor Durkan, Pedro J. Gonçalves, David S. Greenberg, and Jakob H. Macke. sbi: A toolkit for simulation-based inference. *Journal of Open Source Software*, 5(52):2505, 2020.
- [75] Pedro J Gonçalves, Jan-Matthis Lueckmann, Michael Deistler, Marcel Nonnenmacher, Kaan Öcal, Giacomo Bassetto, Chaitanya Chintaluri, William F Podlaski, Sara A Haddad, Tim P Vogels, et al. Training deep neural density estimators to identify mechanistic models of neural dynamics. *Elife*, 9:e56261, 2020.
- [76] Michael Deistler, Pedro J Goncalves, and Jakob H Macke. Truncated proposals for scalable and hassle-free simulation-based inference. *arXiv preprint arXiv:2210.04815*, 2022.

- [77] Conor Durkan, Artur Bekasov, Iain Murray, and George Papamakarios. Neural spline flows. *Advances in Neural Information Processing Systems*, 32, 2019.
- [78] Harold V Henderson and SR Searle. Vec and vech operators for matrices, with some uses in jacobians and multivariate statistics. *Canadian Journal of Statistics*, 7(1):65–81, 1979.
- [79] Lawrence I-Kuei Lin. A concordance correlation coefficient to evaluate reproducibility. *Biometrics*, pages 255–268, 1989.
- [80] Nicholas Lange, Stephen C Strother, Jon R Anderson, Finn Å Nielsen, Andrew P Holmes, Thomas Kolenda, Robert Savoy, and Lars Kai Hansen. Plurality and resemblance in fmri data analysis. *NeuroImage*, 10(3):282–303, 1999.
- [81] H R Wilson and J D Cowan. Excitatory and inhibitory interactions in localized populations of model neurons. *Biophysical journal*, 12(1):1–24, 1972.
- [82] Caglar Cakan, Nikola Jajcay, and Klaus Obermayer. neurolib: A simulation framework for whole-brain neural mass modeling. *Cognitive Computation*, pages 1–21, 2021.
- [83] Anton Tokariev, James A Roberts, Andrew Zalesky, Xuelong Zhao, Sampsa Vanhatalo, Michael Breakspear, and Luca Cocchi. Large-scale brain modes reorganize between infant sleep states and carry prognostic information for preterms. *Nature communications*, 10(1):2619, 2019.
- [84] Aaron F Alexander-Bloch, Haochang Shou, Siyuan Liu, Theodore D Satterthwaite, David C Glahn, Russell T Shinohara, Simon N Vandekar, and Armin Raznahan. On testing for spatial correspondence between maps of human brain structure and function. *Neuroimage*, 178:540–551, 2018.
- [85] Paula Sanz-Leon, Stuart A. Knock, Andreas Spiegler, and Viktor K. Jirsa. Mathematical framework for large-scale brain network modeling in The Virtual Brain. *NeuroImage*, 111:385–430, 2015.
- [86] Tristan T. Nakagawa, Mark Woolrich, Henry Luckhoo, Morten Joensson, Hamid Mohseni, Morten L. Kringelbach, Viktor Jirsa, and Gustavo Deco. How delays matter in an oscillatory whole-brain spiking-neuron network model for MEG alpha-rhythms at rest. *NeuroImage*, 87:383–394, 2014.
- [87] Gustavo Deco, Joana Cabral, Mark W. Woolrich, Angus B. A. Stevner, Tim J. van Harteveldt, and Morten L. Kringelbach. Single or multiple frequency generators in on-going brain activity: A mechanistic whole-brain model of empirical meg data. *NeuroImage*, 152:538–550, May 2017.
- [88] S. D. Kulik, L. Douw, E. van Dellen, M. D. Steenwijk, J. J. G. Geurts, C. J. Stam, A. Hillebrand, M. M. Schoonheim, and P. Tewarie. Comparing individual and group-level simulated neurophysiological brain connectivity using the Jansen and Rit neural mass model. *Network Neuroscience*, pages 1–37, 01 2023.
- [89] Romesh G. Abeysuriya, Jonathan Hadida, Stamatios N. Sotiropoulos, Saad Jbabdi, Robert Becker, Benjamin A. E. Hunt, Matthew J. Brookes, and Mark W. Woolrich. A biophysical model of dynamic balancing of excitation and inhibition in fast oscillatory large-scale networks. *PLOS Computational Biology*, 14(2):1–27, 02 2018.
- [90] Prejaas Tewarie, Benjamin AE Hunt, George C O'Neill, Aine Byrne, Kevin Aquino, Markus Bauer, Karen J Mullinger, Stephen Coombes, and Matthew J Brookes. Relationships between neuronal oscillatory amplitude and dynamic functional connectivity. *Cerebral Cortex*, 29(6):2668–2681, 2019.

- [91] Parul Verma, Srikantan Nagarajan, and Ashish Raj. Stability and dynamics of a spectral graph model of brain oscillations. *Network Neuroscience*, pages 1–43, 07 2022.
- [92] Peter A Robinson, CJ Rennie, Donald L Rowe, SC O’Connor, and E Gordon. Multiscale brain modelling. *Philosophical Transactions of the Royal Society B: Biological Sciences*, 360(1457):1043–1050, 2005.
- [93] Walter J Freeman and Jian Zhai. Simulated power spectral density (PSD) of background electrocorticogram (ECoG). *Cognitive Neurodynamics*, 3(1):97–103, 2009.
- [94] Biyu J. He, John M. Zempel, Abraham Z. Snyder, and Marcus E. Raichle. The Temporal Structures and Functional Significance of Scale-free Brain Activity. *Neuron*, 66(3):353–369, 2010.
- [95] H. Shimizu and H. Haken. Co-operative dynamics in organelles. *Journal of Theoretical Biology*, 104(2):261–273, 1983.
- [96] V.K. Jirsa, K.J. Jantzen, A. Fuchs, and J.A.S. Kelso. Spatiotemporal forward solution of the eeg and meg using network modeling. *IEEE Transactions on Medical Imaging*, 21(5):493–504, 2002.
- [97] Gustavo Deco, Mario Senden, and Viktor Jirsa. How anatomy shapes dynamics: a semi-analytical study of the brain at rest by a simple spin model. *Frontiers in Computational Neuroscience*, 6:68, 2012.
- [98] F Abdelnour, A Raj, M Dayan, O Devinsky, and T Thesen. Estimating function from structure in epileptics using graph diffusion model. In *2015 IEEE 12th International Symposium on Biomedical Imaging (ISBI)*, pages 466–469, 2015.
- [99] Erfan Nozari, Jennifer Stiso, Lorenzo Caciagli, Eli J. Cornblath, Xiaosong He, Maxwell A. Bertolero, Arun S. Mahadevan, George J. Pappas, and Danielle S. Bassett. Is the brain macroscopically linear? a system identification of resting state dynamics. *bioRxiv*, 2020.
- [100] Leandro M Alonso and Eve Marder. Visualization of currents in neural models with similar behavior and different conductance densities. *Elife*, 8, 2019.
- [101] Adrian E Raftery and Steven M Lewis. Implementing mcmc. *Markov chain Monte Carlo in practice*, pages 115–130, 1996.
- [102] Stefan Frässle, Ekaterina I. Lomakina, Adeel Razi, Karl J. Friston, Joachim M. Buhmann, and Klaas E. Stephan. Regression DCM for fMRI. *NeuroImage*, 155:406–421, 2017. Publisher: Elsevier.
- [103] Stefan Frässle, Ekaterina I. Lomakina, Lars Kasper, Zina M. Manjaly, Alex Leff, Klaas P. Pruessmann, Joachim M. Buhmann, and Klaas E. Stephan. A generative model of whole-brain effective connectivity. *NeuroImage*, 179:505–529, 2018.
- [104] Arjan Hillebrand and Gareth R. Barnes. Beamformer analysis of MEG data. In *Magnetoencephalography*, volume 68 of *International Review of Neurobiology*, pages 149–171. Academic Press, 2005.
- [105] R.N. Henson, J. Mattout, C. Phillips, and K.J. Friston. Selecting forward models for MEG source-reconstruction using model-evidence. *NeuroImage*, 46(1):168–176, 2009.

- [106] R. Franciotti, D. Iacono, S. Della Penna, V. Pizzella, K. Torquati, M. Onofrj, and G.L. Romani. Cortical rhythms reactivity in ad, lbd and normal subjects: A quantitative meg study. *Neurobiology of Aging*, 27(8):1100–1109, 2006.
- [107] Joan Francesc Alonso, Jesús Poza, MIGUEL Angel MANanas, Sergio Romero, Alberto Fernández, and Roberto Hornero. Meg connectivity analysis in patients with alzheimer’s disease using cross mutual information and spectral coherence. *Annals of biomedical engineering*, 39:524–536, 2011.
- [108] Javier Escudero, Saeid Sanei, Delaram Jarchi, Daniel Abásolo, and Roberto Hornero. Regional coherence evaluation in mild cognitive impairment and alzheimer’s disease based on adaptively extracted magnetoencephalogram rhythms. *Physiological measurement*, 32(8):1163, 2011.
- [109] Kamalini G. Ranasinghe, Leighton B. Hinkley, Alexander J. Beagle, Danielle Mizuiri, Anne F. Dowling, Susanne M. Honma, Mariel M. Finucane, Carole Scherling, Bruce L. Miller, Srikantan S. Nagarajan, and Keith A. Vossel. Regional functional connectivity predicts distinct cognitive impairments in alzheimer’s disease spectrum. *NeuroImage: Clinical*, 5:385–395, 2014.
- [110] Zhengdao Li, Kai Hwang, Keqin Li, Jie Wu, and Tongkai Ji. Graph-generative neural network for EEG-based epileptic seizure detection via discovery of dynamic brain functional connectivity. *Scientific Reports*, 12(1):18998, 2022.
- [111] Escande A. Racine E, Sattler S. Free will and the brain disease model of addiction: The not so seductive allure of neuroscience and its modest impact on the attribution of free will to people with an addiction. *Front Psychol.*, 1(8), Nov 2017.
- [112] Bradl M. Lassmann H. Multiple sclerosis: experimental models and reality. *Acta Neuropathol.*, 133(2):223–244, Feb 2017.
- [113] Carolina Beppi, Inês Ribeiro Violante, Gregory Scott, and Stefano Sandrone. EEG, MEG and neuromodulatory approaches to explore cognition: Current status and future directions. *Brain and Cognition*, 148:105677, 2021.
- [114] Kamalini Ranasinghe, Parul Verma, Chang Cai, Xihe Xie, Kiwamu Kudo, Xiao Gao, Hannah Lerner, Danielle Mizuiri, Amelia Strom, Leonardo Iaccarino, Renaud La Joie, Bruce L Miller, Maria Luisa Gorno-Tempini, Katherine P Rankin, William J Jagust, Keith Vossel, Gil Rabinovici, Ashish Raj, and Srikantan Nagarajan. Altered excitatory and inhibitory neuronal subpopulation parameters are distinctly associated with tau and amyloid in alzheimer’s disease. *eLife*, 11:e77850, may 2022.
- [115] Bruce Fischl, David H Salat, Evelina Busa, Marilyn Albert, Megan Dieterich, Christian Haselgrove, Andre Van Der Kouwe, Ron Killiany, David Kennedy, Shuna Klaveness, Albert Montillo, Nikos Makris, Bruce Rosen, and Anders M Dale. Whole Brain Segmentation : Automated Labeling of Neuroanatomical Structures in the Human Brain. *Neuron*, 33:341–355, 2002.
- [116] Julia P. Owen, Yi-Ou Li, Etay Ziv, Zoe Strominger, Jacquelyn Gold, Polina Bukhpun, Mari Wakahiro, Eric J. Friedman, Elliott H. Sherr, and Pratik Mukherjee. The structural connectome of the human brain in agenesis of the corpus callosum. *NeuroImage*, 70:340–355, 2013.
- [117] Mark Jenkinson, Christian F. Beckmann, Timothy E.J. Behrens, Mark W. Woolrich, and Stephen M. Smith. FSL. *NeuroImage*, 62(2):782–790, 2012.

- [118] Sarang S Dalal, JM Zumer, V Agrawal, KE Hild, Kensuke Sekihara, and SS Nagarajan. Nutmeg: a neuromagnetic source reconstruction toolbox. *Neurology & clinical neurophysiology: NCN*, 2004:52, 2004.
- [119] The Mathworks, Inc., Natick, Massachusetts. *MATLAB version 9.8.0.1451342 (R2020a) Update 5*, 2020.

Supplementary Materials

S.1 Details of Data Processing

MRI A 3 Tesla TIM Trio MR scanner (Siemens, Erlangen, Germany) was used to perform MRI using a 32-channel phased-array radiofrequency head coil. High-resolution MRI of each subject’s brain was collected using an axial 3D magnetization prepared rapid-acquisition gradient-echo T1-weighted sequence (echo time [TE] = 1.64 ms, repetition time [TR] = 2,530 ms, TI = 1,200 ms, flip angle of 7°) with a 256-mm field of view, and 160 1.0-mm contiguous partitions at a 256 × 256 matrix. Whole-brain diffusion-weighted images were collected at $b = 1,000\text{s/mm}^2$ with 30 directions using 2-mm voxel resolution in-plane and through-plane.

Region parcellations The T1-weighted images were parcellated into 68 cortical regions and 18 subcortical regions using the Desikan–Killiany atlas available in the FreeSurfer software [115]. To do this, the subject-specific T1-weighted images were back-projected to the atlas using affine registration, as described in the previous studies [23, 116].

Structural connectivity networks Different structural connectivity networks were reconstructed with the same Desikan–Killiany parcellations. Firstly, openly available diffusion MRI data were obtained from the MGH-USC Human Connectome Project to create an average template connectome. As in previous studies [23, 116], subject-specific structural connectivity was computed on diffusion MRI data: *Bedpostx* was used to determine the orientation of brain fibers in conjunction with *FLIRT*, as implemented in the *FSL* software [117]. In order to determine the elements of the adjacency matrix, tractography was performed using *probtrackx2*. 4,000 streamlines were initiated from each seed voxel corresponding to a cortical or subcortical gray matter structure and how many of these streamlines reached a target gray matter structure was tracked. The weighted connection between the two structures $c_{i,j}$, was defined as the number of streamlines initiated by voxels in region i that reach any voxel within region j , normalized by the sum of the source and target region volumes ($c_{i,j} = \frac{\text{streamlines}}{v_i + v_j}$). Afterward, connection strengths were averaged between both directions ($c_{i,j}$ and $c_{j,i}$) to form undirected edges. To determine the geographic location of an edge, the top 95% of nonzero voxels by streamline count were computed for both edge directions. The consensus edge was defined as the union between both post-threshold sets.

MEG data MEG recordings were acquired at UCSF using a 275-channel CTF Omega 2,000 whole-head MEG system from VSM MedTech (Coquitlam, BC, Canada). All subjects were instructed to keep their eyes closed for 5 min while their MEGs were recorded at a sampling frequency of 1,200 Hz.

MEG processing and source reconstruction MEG recordings were downsampled from 1,200 Hz to 600 Hz, then digitally filtered to remove DC offset and any other noisy artifact outside of the 1 to 160 Hz bandpass range. Since MEG data are in sensor space, meaning they represent the signal observable from sensors placed outside the head, this data needed to be “inverted” in order to infer the neuronal activity that had generated the observed signal by solving the so-called inverse problem. Adaptive spatial filtering algorithms were used from the NUTMEG software tool written in house [118]. To prepare for source localization, all MEG sensor locations were co-registered to each subject’s anatomical MRI scans. The lead field (forward model) for each subject was calculated in NUTMEG using a multiple local-spheres head model (three-orientation lead field) and an 8 mm voxel grid which generated more than 5,000 dipole sources, all sources were normalized to have a norm of 1. Finally, the MEG recordings were projected into the source space using a beamformer spatial filter. Only the sources belonging to the 68 cortical regions were selected to be averaged around the centroid. All dipole sources were labeled based on the Desikan–Killiany parcellations, then sources within a 20 mm radial distance to the centroid of each brain region were extracted, and the average time course of each region’s extracted sources served as empirical resting-state data for our proposed model. MEG recordings were bandpass filtered between 2 to 45 Hz using `firls` in MATLAB [119] and the static frequency PSD was generated for every region of interest using the `pmtm` algorithm in MATLAB [119].

S.2 Spectral Graph Model

Notation All the vectors and matrices are written in boldface and the scalars are written in normal font. The frequency f of a signal is specified in Hertz (Hz), and the corresponding angular frequency $\omega = 2\pi f$ is used to obtain the Fourier transforms. The connectivity matrix is defined as $\mathbf{C} = c_{jk}$, where c_{jk} is the connectivity strength between regions j and k , normalized by the row degree.

Mesoscopic Model

Given region k out of N regions, we denote the local excitatory signal as $x_e(t)$, local inhibitory signal as $x_i(t)$, and the long-range macroscopic signals as $x_k(t)$. Combining the decay of individual signals, coupling of excitatory and inhibitory signals as well as input white Gaussian noise, the evolution models of $x_e(t)$ and $x_i(t)$ are:

$$\frac{dx_e(t)}{dt} = -\frac{f_e(t)}{\tau_e} \star (g_{ee} x_e(t) - g_{ei} f_i(t) \star x_i(t)) + p(t), \text{ and,} \quad (6)$$

$$\frac{dx_i(t)}{dt} = -\frac{f_i(t)}{\tau_i} \star (g_{ii} x_i(t) + g_{ei} f_e(t) \star x_e(t)) + p(t), \quad (7)$$

where $f_e(t)$ and $f_i(t)$ are the ensemble average neural impulse response function, \star stands for convolution, $p(t)$ is input noise, parameters g_{ee} , g_{ii} , g_{ei} are neural gain terms, and parameters τ_e , τ_i are characteristic time constants, which are shared for every region k . We assume Gamma-shaped $f_e(t)$ and $f_i(t)$ as

$$f_e(t) = \frac{1}{\tau_e^2} \exp\left(\frac{-t}{\tau_e}\right) \text{ and } f_i(t) = \frac{1}{\tau_i^2} \exp\left(\frac{-t}{\tau_i}\right).$$

Macroscopic Model

Accounting for long-range connections between brain regions, the macroscopic signal x_k is assumed to conform to the following evolution model:

$$\frac{dx_k(t)}{dt} = -\frac{1}{\tau_G} f_G(t) \star x_k(t) + \frac{\alpha}{\tau_G} f_G(t) \star \sum_{j=1}^N c_{jk} x_j(t - \tau_{jk}^v) + (x_e(t) + x_i(t)), \quad (8)$$

where, τ_G is the graph characteristic time constant, α is the global coupling constant, c_{jk} are elements of the connectivity matrix, τ_{jk}^v is the delay in signals reaching from the j^{th} to the k^{th} region, v is the cortico-cortical fiber conduction speed with which the signals are transmitted. The delay τ_{jk}^v is calculated as d_{jk}/v , where d_{jk} is the distance between regions j and k and $x_e(t) + x_i(t)$ is the input signal determined from Equations (6) and (7). The Gamma-shaped $f_G(t)$ is written as

$$f_G(t) = \frac{1}{\tau_G^2} \exp\left(\frac{-t}{\tau_G}\right).$$

The neural gain g_{ee} is kept as 1 to ensure parameter identifiability, therefore, SGM only includes 7 identifiable parameters as listed in Table 1.

Closed-Form Model Solution in the Fourier Domain

A salient feature of SGM is that it provides a closed-form solution of brain oscillations under the frequency domain. Let \mathcal{F} be the Fourier transform at angular frequency $\omega = 2\pi f$. Note that the mesoscopic models for different regions share the same parameters, therefore, without loss of generality, we can drop the subscript k .

The solutions for $x_e(t)$ and $x_i(t)$ under the frequency domain are

$$X_e(\omega) = \mathcal{F}(x_e(t)) = \frac{\left\{1 + \frac{g_{ei}F_e(\omega)F_i(\omega)/\tau_e}{j\omega + g_{ii}F_i(\omega)/\tau_i}\right\} P(\omega)}{j\omega + g_{ee}F_e(\omega)/\tau_e + \frac{(g_{ei}F_e(\omega)F_i(\omega))^2}{\tau_e\tau_i(j\omega + g_{ii}F_i(\omega)/\tau_i)}} = H_e(\omega)P(\omega),$$

and

$$X_i(\omega) = \mathcal{F}(x_i(t)) = \frac{\left\{1 + \frac{g_{ei}F_e(\omega)F_i(\omega)/\tau_i}{j\omega + g_{ee}F_e(\omega)/\tau_e}\right\} P(\omega)}{j\omega + g_{ii}F_i(\omega)/\tau_i + \frac{(g_{ei}F_e(\omega)F_i(\omega))^2}{\tau_e\tau_i(j\omega + g_{ee}F_e(\omega)/\tau_e)}} = H_i(\omega)P(\omega),$$

where $P(\omega)$, $F_e(\omega)$, $F_i(\omega)$, $F_G(\omega)$ are the Fourier transform of $p(t)$, $f_e(t)$, $f_i(t)$, and $f_G(t)$ at angular frequency ω .

We define the complex Laplacian matrix $\mathcal{L}(\omega) = i - \alpha \mathbf{C}^*(\omega)$ where $\mathbf{C}^*(\omega) = [c_{ij} \exp(-j\omega\tau_{ij}^v)]_{i,j=1,\dots,N}$. The solution of the macroscopic signals at a angular frequency ω is

$$\mathbf{X}(\omega) = [\mathcal{F}(x_1(t)), \dots, \mathcal{F}(x_N(t))]^\top = \left(j\omega + \frac{1}{\tau_g} F_g(\omega) \mathcal{L}(\omega)\right)^{-1} H_{\text{local}}(\omega) \mathbf{P}(\omega), \quad (9)$$

where $H_{\text{local}}(\omega) = H_e(\omega) + H_i(\omega)$.

From here, we can re-write $\mathbf{X}(\omega)$ by using the eigendecomposition of the complex Laplacian matrix $\mathcal{L}(\omega)$ which is:

$$\mathcal{L}(\omega) = \mathbf{U}(\omega)\Lambda(\omega)\mathbf{U}(\omega)^H, \quad (10)$$

where, $\mathbf{U}(\omega)$ are the eigenvectors and $\Lambda(\omega) = \text{diag}([\lambda_1(\omega), \dots, \lambda_N(\omega)])$ consist of the eigenvalues $\lambda_1(\omega), \dots, \lambda_N(\omega)$, at angular frequency ω .

By using the above eigen-decomposition of the Laplacian matrix, the $\mathbf{X}(\omega)$ can be re-written as:

$$\mathbf{X}(\omega) = \sum_{k=1}^N \frac{\mathbf{u}_k(\omega)\mathbf{u}_k(\omega)^H}{j\omega + \tau_G^{-1}\lambda_k(\omega)F_G(\omega)} H_{\text{local}}(\omega)\mathbf{P}(\omega), \quad (11)$$

where, $\mathbf{u}_k(\omega)$ are the eigenvectors from $\mathbf{U}(\omega)$ and $\lambda_k(\omega)$ are the eigenvalues from $\Lambda(\omega)$ obtained by the eigen-decomposition of the Laplacian matrix $\mathcal{L}(\omega)$ obtained in Eq. (10). Equation (11) is the closed-form steady state solution of the macroscopic signals at a specific angular frequency ω . As SGM provides a closed-form solution $\mathbf{X}(\omega)$, we can compare the modeled and empirical power spectra to estimate the global parameters.

S.3 More Plots

- **Individual-Level Results:** While in the main text we focus on group-level results, we also provide individual-level results in Figure S1 and Figure S2. We select two representative subjects to show the individual-level results. Specifically, we choose the subjects with the Pearson's correlation between the empirical FC and model-predicted (SGM-SBI model) FC closest to the mean of all subjects on *alpha* band.
- **Other metrics results:** Figure S3 shows the original MSE, original Lin's correlation and standardized Pearson's correlation between the empirical FC and model-predicted FC as the supplementary for Figure 5.
- **MSE versus parameters:** Figure S4 shows the average MSE across 36 subjects between the empirical FC and model-predicted FC using the SGM-SBI model for different values of the SGM parameters. For each parameter, we vary it and fix the others to the optimal values obtained from the SBI algorithm. The red dashed lines represent the boundaries we used as indicated in Table 1.

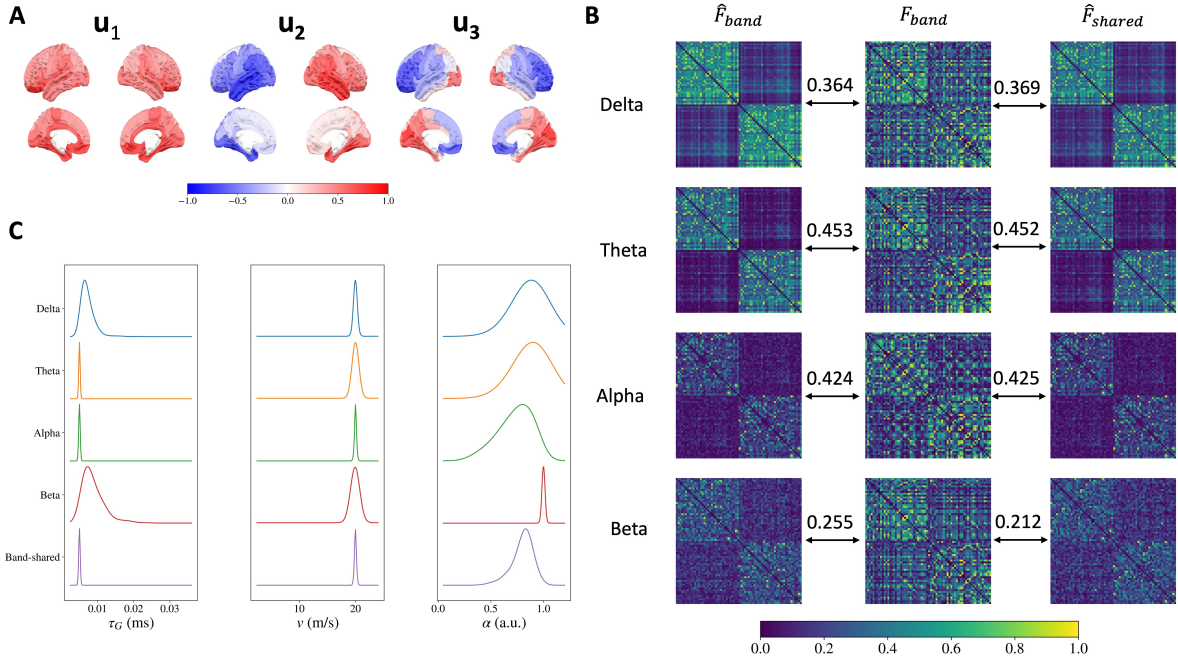


Figure S1: Results from the first representative subject. **A:** The real part of first three complex Laplacian eigenvectors at the *alpha* band plotted on the brain. **B:** Mean estimated FCs for *delta*, *theta*, *alpha* and *beta* bands from the SGM-SBI model (left), empirical FCs (middle) and SGM-SBI-shared model (right). The numbers above the arrows represent the average Pearson's correlation between estimated and empirical FCs. **C:** The posterior density plots of the SGM parameters estimated by fitting empirical FCs with SGM-SBI for *delta*, *theta*, *alpha*, *beta* bands and with SGM-SBI-shared method via stacking FCs from 4 bands together. The SGM parameters include graph time constant τ_g (left), transmission speed v (middle) and coupling constant α (right). For better visualization, all the density curves are normalized such that they have the same peak value.

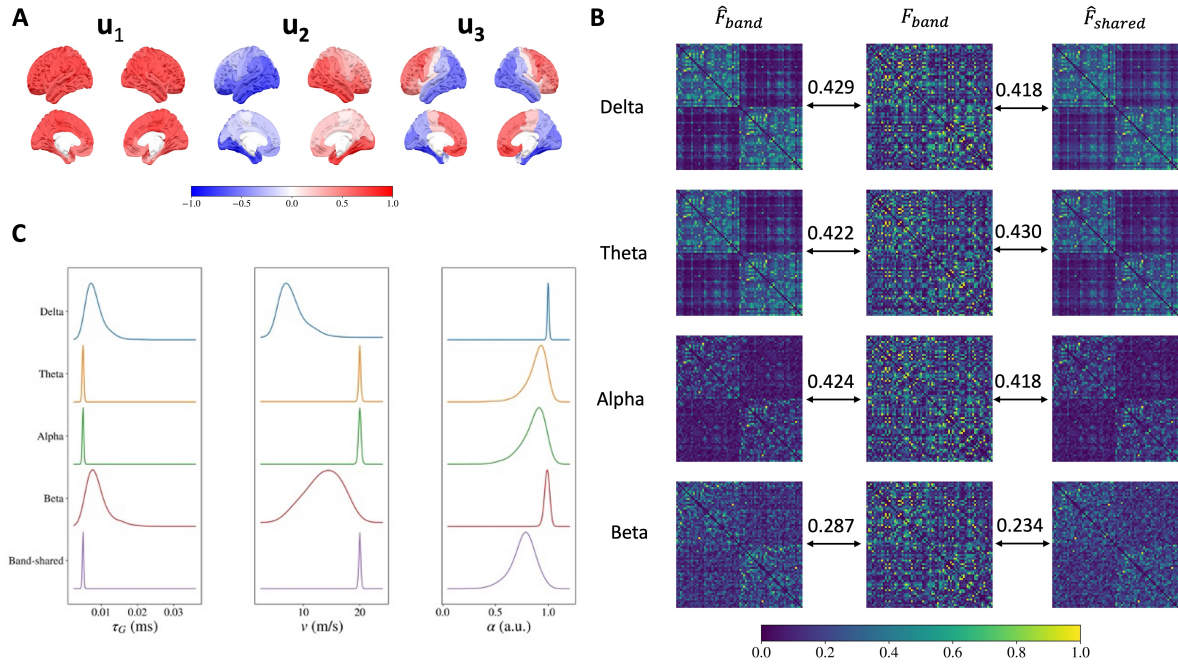


Figure S2: Results from the second representative subject. **A:** The real part of first three complex Laplacian eigenvectors at the *alpha* band plotted on the brain. **B:** Mean estimated FCs for *delta*, *theta*, *alpha* and *beta* bands from the SGM-SBI model (left), empirical FCs (middle) and SGM-SBI-shared model (right). The numbers above the arrows represent the average Pearson's correlation between estimated and empirical FCs. **C:** The posterior density plots of the SGM parameters estimated by fitting empirical FCs with SGM-SBI for *delta*, *theta*, *alpha*, *beta* bands and with SGM-SBI-shared method via stacking FCs from 4 bands together. The SGM parameters include graph time constant τ_g (left), transmission speed v (middle) and coupling constant α (right). For better visualization, all the density curves are normalized such that they have the same peak value.

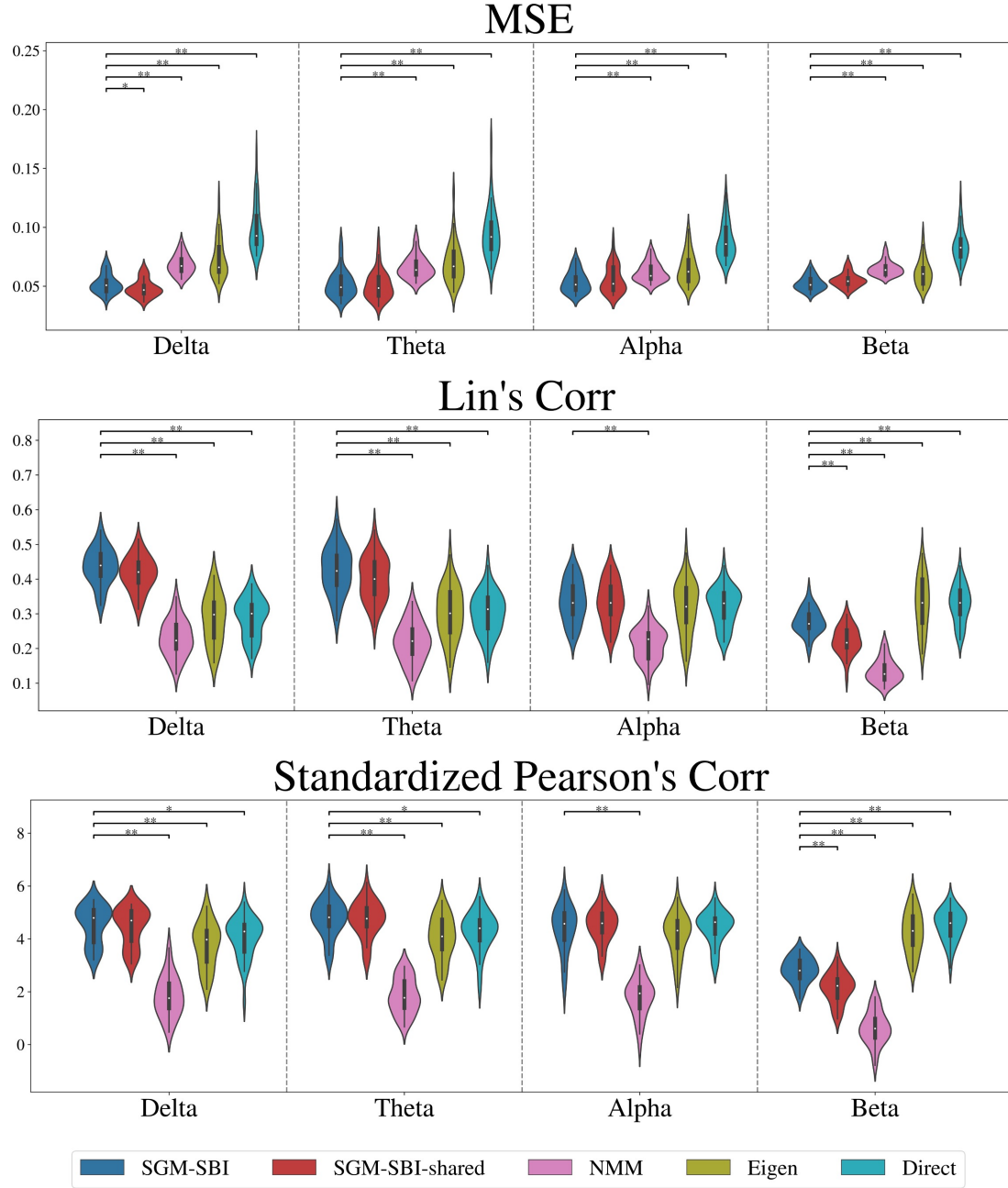


Figure S3: Violin plots of MSE (top), Lin's correlation (middle) and standardized Pearson's correlation (bottom) between the empirical FC and model-predicted FC using five competing models: SGM-SBI, SGM-SBI-wGeo, SGM-SBI-shared, SGM-SBI-shared-wGeo, NMM, eigen-mapping and direct mapping for *delta*, *theta*, *alpha* and *beta* bands. We aim to assess the performance of different methods on reproducing the empirical MEG FC matrices and use three metrics, MSE (the lower the better), Lin's correlation (the higher the better) and Pearson's correlation (the higher the better). Direct mapping refers to the simple correlation or MSE between SC and FC. We show the significant Student's t-test results comparing SGM-SBI with other methods. “*” indicates the test result with a p-value within [0.001, 0.05] and “**” indicates the test result with a p-value < 0.001.

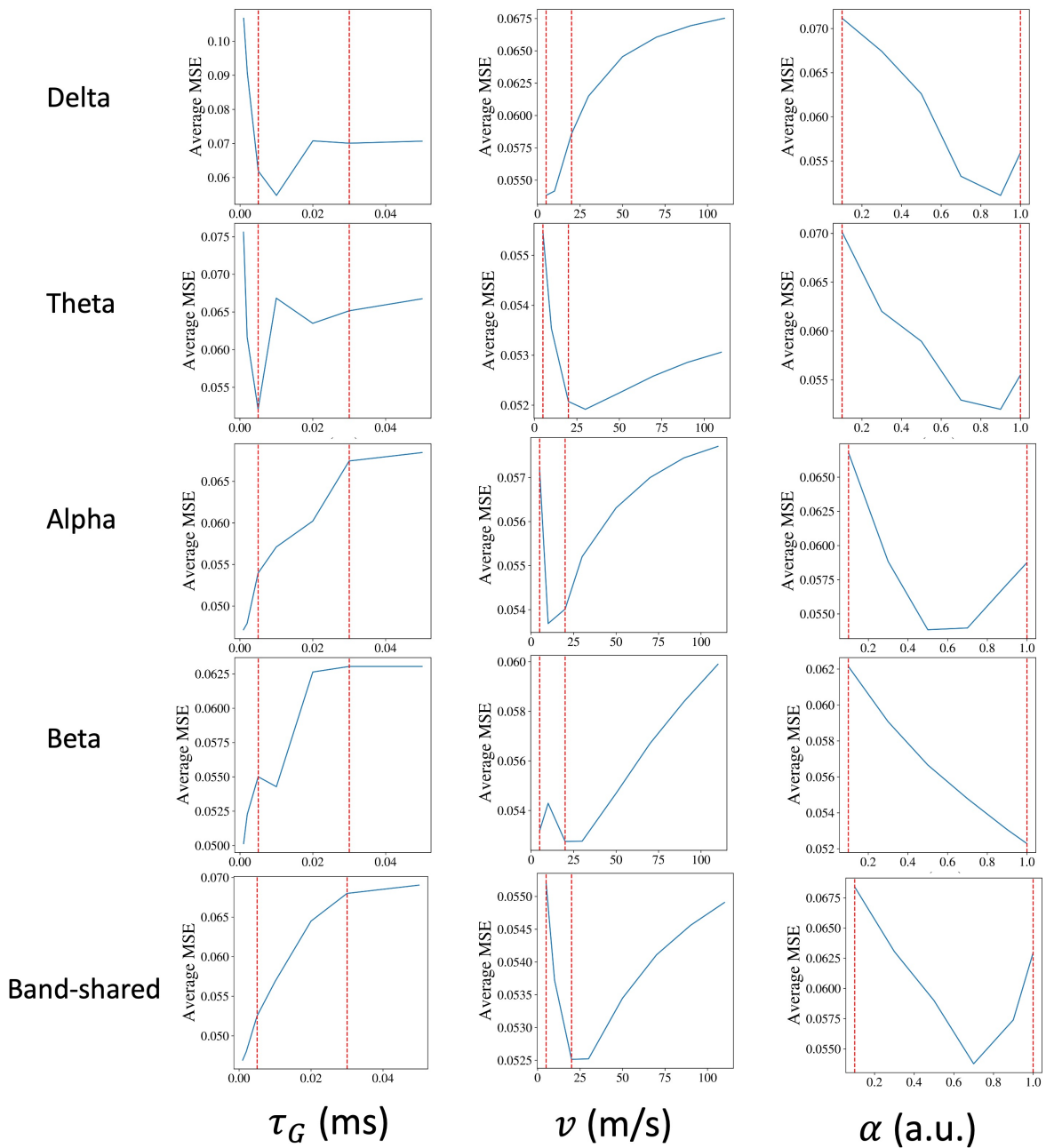


Figure S4: Average MSE across 36 subjects between the empirical FC and model-predicted FC using the SGM-SBI model for different values of the SGM parameters. For each parameter, we vary it and fix the others to the optimal values obtained from the SBI algorithm. The red dashed lines represent the boundaries we used as indicated in Table 1.